UNIVERSITÀ
DI PAVIA

UNIVERSITY OF PAVIA

FACULTY OF ENGINEERING

DEPARTMENT OF ELECTRICAL, COMPUTER AND BIOMEDICAL ENGINEERING

MASTER'S DEGREE IN ELECTRICAL ENGINEERING

MASTER THESIS

TITLE (English)

Investigation of Surface Slotting in Additively Manufactured Rotors with Respect to Eddy-Current Suppression and Manufacturability

TITOLO (Italiano)

Studio della scanalatura superficiale di rotori realizzati mediante manifattura additiva in relazione alla soppressione delle correnti parassite e alla fabbricabilità

Candidate: Yousef Ahmadi

Supervisor: Prof. Piero Malcovati

Erasmus+ Traineeship Supervisor: Mr. Marius Behrendt

A.A. 2025/2026

Abstract in English

Additive manufacturing enables new rotor geometries for electrical machines and offers greater geometric freedom than conventional manufacturing routes. However, solid or weakly segmented rotor structures are generally more susceptible to eddy-current formation than conventional laminated designs. These additional losses can deteriorate efficiency, thermal behavior, and overall electromagnetic performance. Within this context, this thesis investigates surface slotting as a rotor design strategy for reducing eddy-current effects in additively manufactured rotors while maintaining acceptable machine performance and considering manufacturability constraints. In particular, the work focuses on alternative surface-slot patterns beyond simple conventional slits and evaluates their suitability for electromagnetic screening and practical implementation.

The study is carried out using a consistent three-dimensional finite-element-method framework in JMAG. A baseline rotor without advanced surface patterning is first defined as a reference configuration. On this basis, several slot-pattern geometries are modeled and compared, including axial slit arrangements, snake-line slotting, and Hilbert-type surface structures. The comparative assessment is performed under identical modeling assumptions and excitation conditions in order to isolate the influence of surface topology on rotor electromagnetic behavior. The main evaluation criterion is rotor eddy-current losses, while average torque is considered only as a secondary comparative indicator and is interpreted with caution under the present cylindrical rotor representation.

The thesis therefore contributes a structured comparison of how slot-path geometry, segmentation behavior, and surface complexity influence the trade-off between electromagnetic loss suppression and torque-related performance. Rather than treating surface slotting only as a geometric modification, the work frames it as a design variable linking electromagnetic functionality with additive-manufacturing feasibility. The results provide a screening-oriented basis for identifying promising rotor surface patterns for future development of additively manufactured electrical machines. Overall, the thesis demonstrates that surface structuring can be used to modify rotor eddy-current behavior, while the final effectiveness remains strongly dependent on the selected pattern geometry.

Abstract in Italiano

La manifattura additiva consente nuove geometrie del rotore per le macchine elettriche e offre una maggiore libertà geometrica rispetto ai processi di produzione convenzionali. Tuttavia, le strutture di rotore solide o debolmente segmentate sono generalmente più soggette alla formazione di correnti parassite rispetto ai tradizionali design laminati. Queste perdite aggiuntive possono peggiorare l'efficienza, il comportamento termico e le prestazioni elettromagnetiche complessive. In questo contesto, la presente tesi analizza la scanalatura superficiale come strategia di progettazione del rotore per ridurre gli effetti delle correnti parassite nei rotori prodotti mediante manifattura additiva, mantenendo al contempo prestazioni accettabili della macchina e tenendo conto dei vincoli di fabbricabilità. In particolare, il lavoro si concentra su configurazioni alternative di scanalature superficiali oltre alle semplici fessure convenzionali e ne valuta l'idoneità per uno screening elettromagnetico e una possibile implementazione pratica.

Lo studio è condotto utilizzando un quadro coerente di simulazione tridimensionale agli elementi finiti in JMAG. Un rotore di base, privo di pattern superficiali avanzati, viene innanzitutto definito come configurazione di riferimento. Su questa base, vengono modellate e confrontate diverse geometrie di scanalatura, comprese configurazioni a fessure assiali, scanalature snake-line e strutture superficiali di tipo Hilbert. La valutazione comparativa viene eseguita sotto ipotesi di modellazione e condizioni di eccitazione identiche, al fine di isolare l'influenza della topologia superficiale sul comportamento elettromagnetico del rotore. Il criterio principale di valutazione è costituito dalle perdite per correnti parassite nel rotore, mentre la coppia media è considerata solo come indicatore comparativo secondario ed è interpretata con cautela nell'ambito dell'attuale rappresentazione cilindrica del rotore.

La tesi fornisce quindi un confronto strutturato di come la geometria del percorso delle scanalature, il comportamento di segmentazione e la complessità superficiale influenzino il compromesso tra la soppressione delle perdite elettromagnetiche e le prestazioni legate alla coppia. Piuttosto che considerare la scanalatura superficiale soltanto come una modifica geometrica, il lavoro la interpreta come una variabile di progetto che collega la funzionalità elettromagnetica con la fattibilità della manifattura additiva. I risultati forniscono una base orientata allo screening per l'individuazione di configurazioni promettenti della superficie del rotore per il futuro sviluppo di macchine elettriche realizzate mediante manifattura additiva. Nel complesso, la tesi dimostra che la strutturazione superficiale può essere utilizzata per modificare il comportamento delle correnti parassite nel rotore, mentre l'efficacia finale rimane fortemente dipendente dalla geometria del pattern selezionato.

Table of contents

Introduction

1.1 Motivation and Problem Context

The development of electrical machines is increasingly influenced by the combined demand for higher efficiency, greater design flexibility, and more adaptable manufacturing routes. In this context, additive manufacturing (AM) has emerged as a promising enabling technology because it allows the realization of geometries that are difficult, costly, or impractical to produce by conventional methods. For electrical-machine components, this freedom is particularly relevant where local features, non-standard surfaces, and integrated geometric modifications may influence electromagnetic behavior. Accordingly, recent work has identified AM not only as a manufacturing route, but also as a design opportunity for machine components and electromagnetic materials [1].

Among the machine parts that can benefit from this freedom, solid rotors are of particular interest. They offer a comparatively simple bulk structure and allow considerable freedom in shaping the active rotor surface. At the same time, this design freedom is accompanied by an important electromagnetic challenge. Since a solid rotor forms a continuous conductive body, it is inherently more susceptible to eddy-current formation than a laminated structure. Under time-varying magnetic excitation, induced currents can circulate inside the rotor material, causing additional Joule losses and influencing the electromagnetic interaction between stator and rotor. In this sense, the rotor surface is not only a geometric boundary, but also an electromagnetic design variable.

One possible way to influence this behaviour is to introduce structured rotor-surface slotting. Instead of leaving the rotor surface smooth and continuous, the surface may be segmented by defined slot paths that interrupt or redirect near-surface current trajectories. In principle, such segmentation can reduce eddy-current-related dissipation by limiting the conductive paths available for induced currents. Previous studies on segmented or slitted magnetic components support the broader idea that geometric interruption can contribute to AC loss reduction in conductive magnetic bodies.

However, rotor surface slotting cannot be judged on loss reduction alone. Any modification of the rotor surface also changes the local field distribution and may therefore alter torque-related electromagnetic response. A pattern that reduces rotor loss effectively may not necessarily preserve favourable operating behaviour.

This issue becomes more relevant when additive manufacturing is considered as a genuine design enabler rather than merely a fabrication method. AM makes it possible to manufacture not only simple grooves, but also more advanced surface trajectories that would be difficult to realize conventionally. At the same time,

increased geometric complexity should not automatically be interpreted as beneficial. Its effect must be evaluated comparatively and under controlled conditions. For this reason, the present thesis treats rotor surface slotting as a comparative electromagnetic design problem. The central question is whether selected rotor surface patterns can reduce rotor eddy-current-related losses while maintaining acceptable electromagnetic performance, and whether greater geometric complexity necessarily leads to improved behavior.

1.2 Thesis Aim and Scope

The main objective of this thesis is to investigate the electromagnetic effect of rotor surface slotting in an additively manufactured solid rotor using a common and controlled simulation framework. More specifically, the work examines whether structured rotor-surface patterns can mitigate rotor Joule loss while preserving an acceptable torque response. The study is not intended to produce a final optimized industrial design. Instead, it aims to establish a clear comparative understanding of how different surface-pattern concepts influence rotor electromagnetic behavior.

To address this objective, a smooth rotor is first used as the baseline case. Its response provides the reference against which all patterned cases are evaluated. On this basis, three representative surface-pattern families are investigated: an axial ring-slot pattern, a snake-line pattern, and a Hilbert-type pattern. These geometries are intentionally different in character, ranging from comparatively simple segmentation to more intricate path-based surface structuring. Their comparison makes it possible to assess not only whether rotor surface slotting is beneficial in principle, but also whether the pattern trajectory itself influences the balance between loss reduction and torque response.

The present work is intentionally limited to an electromagnetic screening study. The comparison is based primarily on two performance indicators: rotor Joule loss and electromagnetic torque. Rotor Joule loss is used as the main indicator of eddy-current-related dissipation in the conductive rotor body, while torque is included as a complementary measure of electromagnetic operating response. In addition, magnetic flux density contours are used as qualitative support for interpreting the field interaction with the rotor surface in the different cases. A central principle of the study is consistency. All investigated cases are evaluated using the same machine model, operating point, material framework, boundary treatment, and general simulation approach, so that the rotor surface slot pattern remains the only intentional design change across the compared cases. This ensures that the observed differences can be interpreted primarily as a consequence of surface geometry.

The methodology is based on three-dimensional transient magnetic finite-element analysis in JMAG. The machine is represented as a quarter model with rotational periodicity, which preserves the essential

electromagnetic behaviour of the full machine while keeping computational effort manageable. The simulation sequence follows a consistent structure. First, the common reference machine model is defined. Second, the smooth rotor is analyzed to establish the baseline response. Third, a preliminary slot-parameter study is used to determine suitable reference values for slot depth and slot spacing. Once these parameters are fixed, they are applied in the comparative study of the axial ring-slot, snake-line, and Hilbert-type patterns. The analysis of each case follows the same evaluation logic, with transient outputs examined in the quasi-steady region and integral-average values extracted for the selected performance indicators.

At the same time, several aspects remain outside the scope of the thesis. The work does not attempt a full multi-physics optimization and does not quantify manufacturing feasibility, structural integrity, thermal coupling, or long-term mechanical durability. These aspects are clearly relevant in practical rotor development, especially for additively manufactured components, but they are not modeled here. The findings should therefore be interpreted as comparative electromagnetic design insights rather than as final design prescriptions.

The remainder of the thesis is organized as follows. Chapter 2 presents the technical background relevant to the study and defines the evaluation perspective adopted in the thesis. Chapter 3 describes the simulation model and numerical framework used for the investigation, including the reference machine, the transient JMAG setup, and the investigated rotor geometries. Chapter 4 presents the simulation results and their comparative analysis, beginning with the parameter-selection process for slot depth and slot spacing and then evaluating the baseline and patterned cases using rotor Joule loss and torque as the principal comparison metrics. In this way, the thesis moves from problem framing to model definition and finally to comparative electromagnetic evaluation of rotor surface slot-pattern geometries.

Surface Slotting of Additively Manufactured Rotors

2.1 Problem Description: Eddy Currents in Additively Manufactured Solid Rotors

Eddy currents are closed loops of electric current induced in a conductive body when it is exposed to a time-varying magnetic field or moves through a spatially non-uniform field. The induced current density circulates in planes that are perpendicular to the magnetic flux density, producing ohmic losses and an additional magnetic field that distorts the original excitation [3]For a simple conductive sheet of thickness d subjected to a sinusoidal magnetic flux density of peak value $B_{\mathrm{p}}$and frequency f, the classical specific eddy-current power loss can be estimated as

$$P = \frac{\pi^2 d^2 B_{\mathrm{p}}^2 f^2}{6\,\rho_{\mathrm{el}}\,\rho_{\mathrm{m}}}$$

where $\rho_{\mathrm{el}}$is the electrical resistivity and ρ_{m} is the mass density of the material [3]

This expression shows directly that eddy-current losses scale with the square of both thickness and frequency, and with the square of the local flux density.

In electrical machines with laminated stators and solid steel rotors, the rotor behaves as a bulk, magnetically permeable and electrically conductive region into which slot-related space harmonics and high-frequency components of the air-gap field penetrate. The resulting surface-concentrated eddy currents can reach significant power levels and become a dominant loss component, especially in high-speed induction and permanent-magnet machines[2],[3].Finite-element studies show that the eddy-current loss density in such solid rotors is highest near the rotor surface and directly follows the spatial pattern of slot harmonics in the air-gap flux density. [5]

Additive manufacturing (AM) of soft-magnetic steels introduces an additional layer to this problem. Laser powder bed fusion and related processes inherently produce bulk, non-laminated parts with continuous electrical pathways, which promote large eddy-current loops even at moderate frequencies[1],[4]. Measurements of laser powder bed fusion (LPBF) iron–silicon (Fe–Si) materials and additively manufactured (AM) cores consistently report elevated AC loss coefficients compared with conventional electrical steels, due to process-induced microstructures, porosity and residual stresses [7], [8].When such AM materials are used to manufacture solid rotors, the combination of bulk geometry and AM-specific material properties leads to particularly critical rotor-surface eddy-current losses, making targeted suppression strategies essential [3], [9].

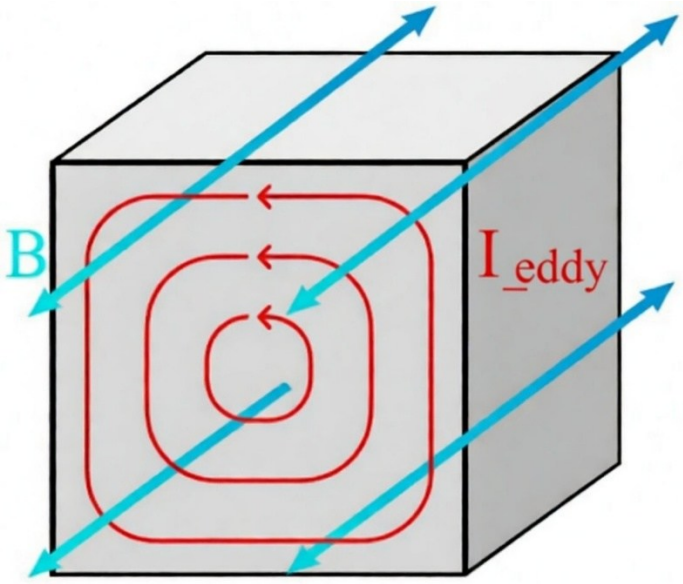

Figure 1 : Schematic illustration of eddy-current loops induced in a conductive solid under a time-varying magnetic flux density B[3]

2.1.1 Difference between Laminated and Solid Rotors

Laminated rotor and stator cores consist of thin, electrically insulated steel sheets that interrupt conductive paths and confine eddy-current loops to the lamination thickness d. Since eddy-current loss scales approximately with d^2, laminations achieve low AC losses even at higher frequencies (Klein et al., 2024), though at the cost of higher manufacturing complexity and reduced geometric flexibility (Goodall et al., 2023). In contrast, solid rotors provide continuous conductive paths, allowing larger eddy-current loops and therefore higher loss densities, typically concentrated near the rotor surface under stator-slot harmonic excitation (Bárta, 2016; Chou et al., 2020). At high frequency, rotor losses increase strongly ($\propto f^2$), making rotor heating and temperature-dependent resistivity relevant (Bílek et al., 2025).Because metal-AM processes typically produce solid cores rather than insulated laminations, AM rotor concepts often rely on geometric segmentation (e.g., voids or thin-wall structures) to mimic lamination effects, within minimum feature-size and tolerance constraints [3], [6], [10].

2.1.2 Observed Surface Eddy-Current Losses and Their Impact on Operating Behaviour

In machines with solid steel rotors, the conductive rotor can support induced current loops driven by air-gap field harmonics. Time-stepping finite-element studies report that the resulting Joule-loss density is typically highest near the rotor surface and often peaks underneath stator slots, consistent with harmonic excitation patterns in the air gap [4], [5].

From a design perspective, rotor eddy-current losses matter because they directly translate into heat generation in the rotor body, which can become a dominant loss component in high-speed operation [4]. This heating is

not only an efficiency penalty; it can also create strong thermal gradients near the surface and affect electrical resistivity, introducing temperature-dependent feedback; in general, higher electrical resistivity tends to reduce induced eddy currents and associated Joule losses, although the net thermal impact must be evaluated [11]. These points motivate focusing on surface-local suppression strategies, since the most critical loss densities are commonly concentrated near the rotor surface [5].

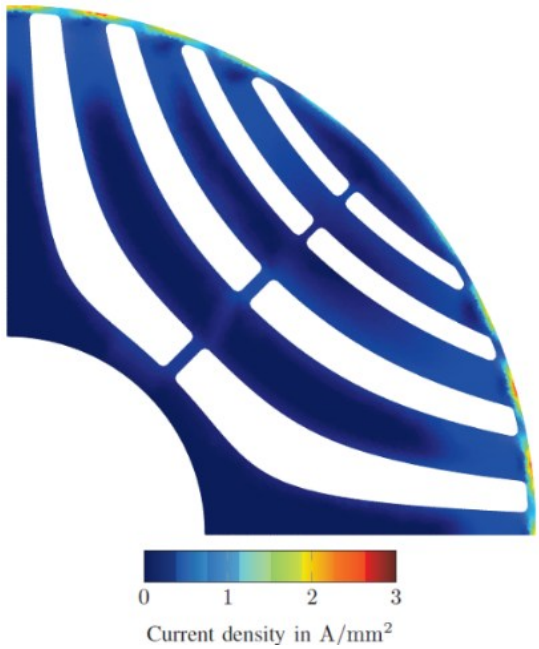

Figure 2: Example of rotor eddy-current density (rms, f = 900 Hz) in the additively manufactured synchronous reluctance reference model, showing that the highest eddy-current densities occur close to the rotor surface and around the flux-barrier intersections, mainly caused by the stator slotting[9].

2.1.3 Motivation for Surface Slotting and Alternative Slotting Concepts

Because eddy currents in solid and AM rotors are predominantly surface-located, many authors propose modifying only the rotor surface to break the azimuthal current paths, rather than attempting full internal lamination. Circumferential slots, axial slits, and combined patterns introduce high-resistance paths that segment the rotor surface into narrower conductive sections, analogous to reducing lamination thickness in a stacked core [4], [11]. In AM synchronous reluctance rotors, circumferential surface slotting has been shown to significantly reduce rotor eddy-current losses by interrupting the current paths created by stator slot harmonics, while keeping the internal flux-barrier structure unchanged [9].

Quantitative studies on additively manufactured reluctance machines demonstrate that the slot spacing acts similarly to the sheet thickness in laminated machines: decreasing spacing between circumferential slots reduces eddy-current losses, while slot depth saturates beyond a certain value due to the finite penetration

depth of the magnetic field [9]. However, deeper slots and reduced surface area increase the effective air-gap length and lead to higher local saturation, which can reduce average torque and affect torque ripple [9] .This trade-off between loss reduction and electromagnetic performance is central to the design of surface-slotting patterns.

Additive manufacturing enables more complex surface-structuring concepts than simple straight slots. Space-filling-curve-based patterns (e.g., Hilbert-type structures) and thin-wall geometries have been explored for soft-magnetic cores to simultaneously reduce eddy-current losses and maintain a high magnetic fill factor. [3], [6]These works show that geometry can be at least as important as material composition in determining the eddy-current loss coefficient of AM parts, and they motivate the application of advanced surface-slotting and space-filling patterns to additively manufactured solid rotors.

2.2 Additively Manufactured Soft-Magnetic Rotor Components

Additive manufacturing (AM) of soft-magnetic cores has progressed from generic material coupons to machine-level demonstrators such as induction motors, axial-flux switched reluctance machines, and transformers, which proves that AM cores are now mature enough to be considered for rotor applications in electrical machines.[1], [9], [12].

At the same time, AM cores still exhibit higher losses and lower permeability than state-of-the-art electrical steels, mainly due to porosity, residual stress, and non-ideal alloy design, so any rotor concept that relies on AM must explicitly account for the coupled constraints of process, material properties, and achievable geometry. [8], [13].

For surface-slotted solid rotors, these three aspects are tightly linked: the chosen AM process (e.g., laser powder bed fusion), the resulting microstructure and magnetic behaviour of Fe–Si or Fe–Ni based alloys, and the minimum printable slot width or wall thickness together determine which slotting concepts are practically feasible and how far eddy-current losses can be reduced. [8], [12].

2.2.1 Metal Additive Manufacturing (L-PBF / SLM) for Rotor Production

For metallic soft-magnetic cores, the dominant additive manufacturing route is laser powder bed fusion (L-PBF), often referred to as selective laser melting (SLM). In L-PBF, thin powder layers (on the order of tens of micrometers) are selectively melted by a scanning laser and consolidated layer-by-layer into a near-net-shape component. Compared with conventional lamination-based manufacturing, L-PBF enables substantially higher geometric freedom, allowing complex three-dimensional flux-guiding features, internal cavities, and integrated cooling concepts that are particularly relevant for rotor designs with flux barriers or

surface structuring. [8], [12].

L-PBF has been demonstrated for soft-magnetic material families relevant to electrical machines (e.g., Fe–Si, Fe–Ni, Fe–Co), including high-silicon Fe–Si compositions that are difficult to process via conventional rolling but can be realized through AM and post-processing[8], [10], [12].

Beyond material coupons, machine-level demonstrators (e.g., induction motors, permanent-magnet synchronous machines (PMSMs), synchronous reluctance motors (SynRMs), transformers, and switched-reluctance prototypes) indicate a trend from material exploration toward system-integrated AM cores, although losses typically remain higher than for state-of-the-art laminated electrical steels. [1], [8], [12]. Alternative AM routes exist, but L-PBF is currently the most promising for dense, load-bearing rotor structures in combination with fine geometric resolution. Binder jetting can offer benefits for eddy-current mitigation via increased resistivity, but involves sintering with substantial dimensional shrinkage, complicating tight rotor tolerances. [12], [14]. Directed energy deposition (DED) supports larger build volumes but often requires extensive post-machining due to microstructure and surface-quality limitations. [8], [12]. For these reasons, and consistent with broader surveys of AM for electrical machines, L-PBF is used as the reference AM process in this work, and its process-dependent geometric limits directly bound feasible slot widths and wall thicknesses for rotor surface structuring. [8], [14].

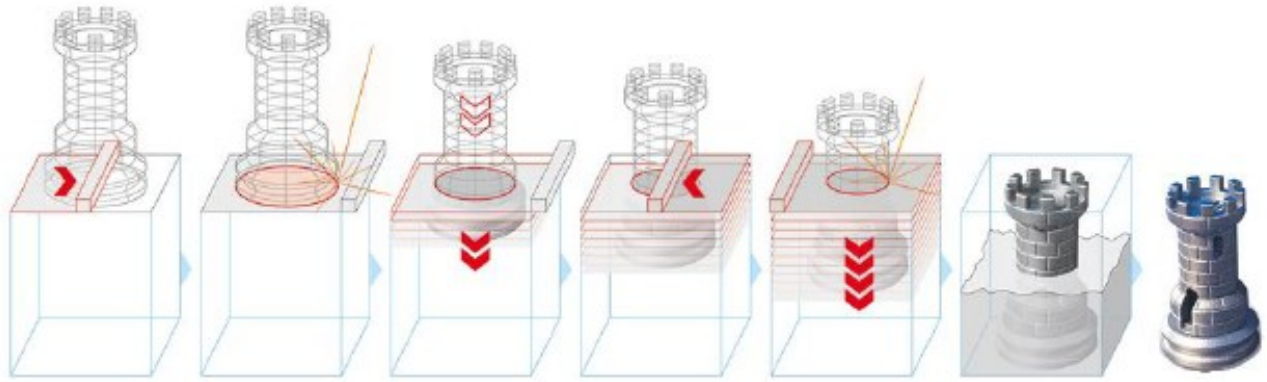

Figure 3: Schematic of the L-PBF process for metallic soft-magnetic parts, showing the laser scanning over a powder bed, successive layers, and the resulting dense core, together with a photograph of printed soft-magnetic test coupons(Reprinted from [2]).

2.2.2 Magnetic and Electrical Properties of AM Soft-Magnetic Steels

Key AM soft-magnetic properties include the relative permeability μ_r, saturation flux density B_{sat}, coercive field H_c, specific magnetic loss P_ϕ, and electrical resistivity ρ_{el}. These parameters depend strongly on the AM process window, heat treatment, and alloy composition. Compared with laminated electrical steels, AM parts

often exhibit higher losses and, in some cases, lower permeability, primarily due to process-induced microstructure/texture effects, residual stresses, and defects such as porosity. Porosity reduces the effective magnetic cross-section and can degrade permeability; its net influence on eddy-current loss can be mixed because an increase in resistivity tends to reduce induced eddy currents, while magnetic degradation can increase overall loss [8], [13].

For L-PBF Fe–Si, reported B_{sat}values are typically in the range of 1.5–1.7 T and $\mu_r It$ is commonly in the hundreds to low thousands; however, hysteresis and eddy-current losses remain higher than in optimized laminations. AM soft-magnetic materials span several families (Fe–Si, Fe–Ni, Fe–Co, ferrites, and composites): metallic alloys can achieve higher saturation, whereas ferrites and composites provide higher resistivity and lower eddy-current losses. Controlling build-direction effects and defects is therefore essential to achieve reproducible electromagnetic performance. [8], [12], [13].

A practical consequence is reduced magnetic fill factor k_{fill}: laminated cores can reach ≈ 0.96, Air-gapped printed cores can be ≈ 0.60, and optimized SLM E-type cores up to ≈ 0.89, which reduces torque density and increases reliance on geometry optimization[1]. Higher ρ_{el} can help reduce eddy-current losses, but porosity/microcracks can reduce effective flux area and weaken thin bridges/slot webs; since L-PBF cores still have higher total losses at high speed/frequency, geometric measures (slotting/structuring) are needed to compensate [8], [13], [14].

2.2.3 Geometric Limits Relevant for Surface Slotting

For surface-slotted AM rotors, not every electromagnetically attractive geometry can be manufactured reliably. The practical design space is constrained by minimum slot width, minimum web/bridge thickness, overhang/support feasibility, and achievable tolerances, all of which depend on the AM process window and build strategy. L-PBF thin-wall studies indicate that ~100 µm walls can be achieved in optimized test conditions, but success depends strongly on build orientation and support strategy; below this range, lack-of-fusion and incomplete track formation become dominant. For rotor bridges and slot webs, such defects are unacceptable because these features must withstand operational loads (e.g., centrifugal forces)[8], [15].

At the component level, AM electrical-machine cores report similar practical limits: minimum tooth tips, yoke segments, and web thicknesses typically remain on the order of a few hundred μm to avoid warping, incomplete fusion, and mechanical failure [1]. Post-processing steps (e.g., stress relief and machining) must be considered, since distortion and material removal can reduce the effective thickness of narrow bridges by tens of μm [1], [8]. Design guidelines, therefore, often relate minimum feature size to process scales (layer thickness and melt-pool diameter), recommending wall thicknesses of at least 3–5× the layer thickness and

slot widths large enough to maintain stable melt pools and enable powder removal [8]. Finally, geometric limits are also functional: bridges are primarily required for mechanical integrity under centrifugal loading; magnetically, they are often designed to operate close to saturation to limit leakage flux, while still satisfying minimum printable thickness and safety margins. At the same time, typical L-PBF tolerances for small features (tens of μm, e.g., ~50 μm without extensive finishing) must be compatible with rotor air-gap and balance requirements [1], [8], [12]. More generally, systematic distortions and shrinkage (e.g., sintering shrinkage in binder jetting and warping from residual stresses in L-PBF) must be compensated during design, which becomes critical for thin webs and high-aspect-ratio slot geometries [8], [14].

2.3 Theoretical Background of Surface Eddy-Current Suppression

In high-speed solid-rotor induction machines and permanent-magnet machines, rotor eddy-current losses can represent a major share of total losses at high rotational speeds and high supply frequencies.[11], [16], [17], [18]In solid-rotor induction motors, the rotor is a continuous conducting body without lamination, so time-varying air-gap fields induce circulating currents that cause significant rotor losses and temperature rise. [18], [19], [20]. High-speed PM machine studies similarly show that rotor eddy-current losses are critical for thermal design and can affect efficiency and reliability. [21], [22], [23], [24].

Overall, surface eddy-current losses are mainly governed by skin effect, the harmonic content of the air-gap flux density, and the rotor surface topology that either enables large current loops or fragments them. [11], [20], [25], [26], [27].

2.3.1 Skin Effect and Penetration Depth in Solid Rotors

Frequency-dependent decomposition of losses in high-speed solid-rotor machines clearly shows that the eddy-current loss component grows rapidly with electrical frequency. [5], [16], [17], [21].

For a high-speed solid-rotor induction machine, Barta expresses the total machine losses as a polynomial in angular frequency ω,

$$P_{loss}(\omega) \approx k_{fund} + k_{hyst}\omega + k_{eddy}\omega^2 + k_{fric}\omega^3,$$

where k_{fund} represents frequency-independent losses, $k_{\text{hyst}}\omega$ hysteresis-related losses, $k_{\text{eddy}}\omega^2$ eddy-current losses, and $k_{\text{fric}}\omega^3$ friction and windage contributions [5]. This form highlights the common scaling that eddy-current losses rise approximately with ω^2, which becomes critical in high-speed operation.

In addition to increasing magnitude, eddy currents at higher frequency become increasingly surface-localized

due to the skin effect. In harmonic-based analyses of solid rotors, the current distribution associated with each harmonic can be characterized using a frequency-dependent penetration depth δ_n [25].

Under classical skin-effect assumptions, the penetration depth for a harmonic component at electrical frequency $f_n$can be approximated as [25]:

$$\delta_n \approx \sqrt{\frac{1}{\pi f_n \mu_0 \mu_r \sigma}} = \sqrt{\frac{2}{w_n \mu_0 \mu_r \sigma}} \quad \omega_{\mathrm{n}} = 2\pi f_n$$

where $\mu_0$is the vacuum permeability, $\mu_r$is the relative permeability of the rotor material, and $\sigma$is the electrical conductivity. The equation shows that increasing harmonic frequency reduces δ_n, concentrating induced currents (and thus Joule losses) closer to the rotor surface. In ferromagnetic steels, $\mu_r$is field-dependent and decreases under saturation; therefore, $\delta_n$should be interpreted as a local, indicative measure rather than a fixed constant [21], [25], [26].

Reported results for solid-rotor induction motors further confirm that at high slip and high frequency, magnetic flux and eddy currents are confined to a thin surface layer, producing large rotor eddy-current losses. [19], [21]. This surface localization also has modeling implications: at higher frequencies (e.g., hundreds of hertz), finite-element models must resolve the penetration depth adequately (e.g., with multiple elements across the effective skin layer) to avoid under- or over-estimating rotor losses. Finally, magnetization conditions near the surface (including DC bias and minor-loop behavior) can influence surface loss predictions, indicating that simplified loss models may be inaccurate if local magnetization history is ignored. [17], [20].

2.3.2 Impact of Air-Gap Harmonics on Surface Losses (Time and Space Harmonics)

Although the fundamental air-gap field mainly produces average torque, it is not necessarily the dominant contributor to rotor-surface eddy-current losses. In particular, near synchronous operation, the fundamental flux-density wave is approximately stationary in the rotor reference frame (effective rotor frequency. ≈ 0) and therefore induces little to no rotor current. In contrast, higher-order space and time harmonics remain asynchronous with respect to the rotor and can dominate rotor-surface induced currents and Joule losses.

Space harmonics arise primarily from stator slotting and other spatial non-idealities, and reducing harmonic content in the air-gap flux can significantly reduce rotor losses in solid-rotor induction machines. [16]. Harmonic-based models show that each harmonic contributes according to its amplitude and frequency, with harmonic-dependent penetration behavior. [25], while 3D FE studies confirm that harmonic spatial distribution directly shapes surface current loops and their losses [26].

Time harmonics are strongly influenced by the inverter supply (PWM). PWM-generated voltage harmonics can substantially increase rotor eddy-current losses, and different modulation strategies yield different spectra and loss levels [23]. Harmonic-rich supplies similarly exacerbate loss and heating in high-speed motors [21]. Field-modulation approaches identify dominant harmonic orders driving PM losses and show that local harmonic environments can create strongly non-uniform current distributions relevant to thermal prediction [22], [28]. More generally, analytical and hybrid methods typically use Fourier representations and explicitly incorporate harmonics in loss calculations, reinforcing that harmonic-spectrum control is central to mitigating rotor surface eddy-current losses [11], [20], [21].

2.3.3 Influence of Rotor Surface Geometry on Eddy-Current Paths Beyond Material Properties

Beyond material properties and harmonic excitation, rotor surface geometry determines how eddy-current loops close and where loss density concentrates. [11], [22], [24], [26], [27]In smooth solid rotors, high-frequency currents tend to form large, low-resistance near-surface loops. Introducing axial slits, tangential grooves, or surface slots can interrupt these loops and increase the effective path resistance; however, the outcome is geometry- and harmonic-dependent, and axial slits can, in some cases, enlarge eddy-current paths and increase local losses. Therefore, the net effect must be verified for the specific harmonic spectrum and operating point. [11], [26], [27]. Analytical work also indicates that slotting modifies dominant current paths and can reduce losses when appropriately designed [20].

The effect is pattern- and parameter-dependent and can be non-monotonic: gains from loop interruption can be offset by leakage and unfavorable harmonic interactions if slot geometry is poorly selected. [17]. In PM-machine studies, slits/slots reduce high current-density concentrations and can significantly reduce rotor losses, but accurate prediction may require 3D modeling to capture end effects and non-uniform distributions. [22], [27]. Using AM-enabled surface grooving patterns, studies also show that geometry can *redistribute* eddy-current paths (including shifting currents into subsurface regions) rather than only reducing their magnitude, and similar segmentation concepts have been used to reduce rotor-shaft losses in high-speed PMSMs [24]. Overall, rotor surface structuring is a strong lever to suppress surface eddy-current losses by cutting, rerouting, or redistributing eddy-current paths under harmonic-rich excitation. [11], [17], [26].

As illustrated in Figure 4, Canseven et al. show that introducing tangential slits in a PMSM rotor core reduces high current-density concentrations compared with a smooth solid core. This indicates that surface segmentation can redistribute near-surface eddy-current paths and thereby mitigate rotor Joule losses, while accurate loss prediction for slitted rotors may require 3D modeling to capture end effects. [27].

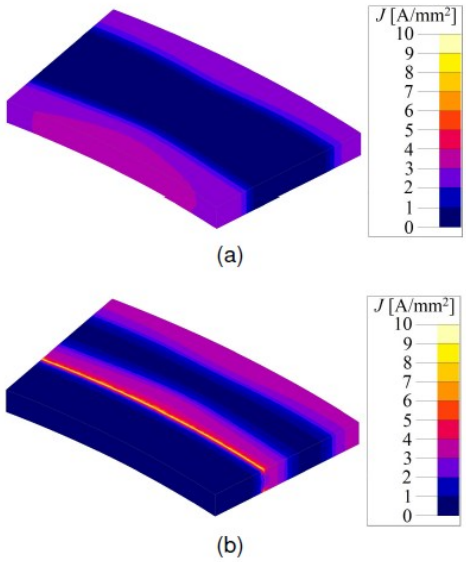

Figure 4: Current density distribution of the prototyped (a) smooth solid core and (b) slitted solid core[27].

2.4 Scope and evaluation criteria for electromagnetic comparison

Additive manufacturing expands the design space (e.g., integrated features and unconventional topologies), but it also introduces constraints that can influence surface structuring, including build-orientation dependence, support strategy, surface quality, distortion risk, and post-processing requirements [26], [29].In addition, slotting may raise mechanical concerns under centrifugal loading, due to stress amplification and stress concentration at groove roots [26], [30], [31].

However, the objective of this thesis is an electromagnetic screening study of slot-pattern geometries. Therefore, manufacturability- and mechanics-related aspects are treated as relevant constraints, but they are not quantified in the present work. The comparative assessment is limited to electromagnetic performance indicators, namely rotor Joule (eddy-current) losses and torque-related quantities extracted from the FE solution (average torque and torque ripple, using a consistent sign convention), under a consistent simulation setup. This scope definition ensures methodological traceability and enables reproducible comparisons across multiple candidates [30], [32], [33]. The considered patterns include axial slits, snake-line, and Hilbert-type surface slotting geometries.

2.4.1 Design-for-AM Constraints for Surface Slotting

For metal powder bed fusion (e.g., L-PBF/SLM), geometric feasibility is governed not only by nominal “printability” but also by distortion control, support accessibility, and post-processing viability. Build orientation is a first-order variable because dimensional accuracy and feature definition are direction-

dependent, which is particularly relevant for near-surface slot features in rotor active parts [26].

Support structures may be necessary to limit deformation during printing, but supports near functional air-gap surfaces are problematic because support removal and subsequent finishing can compromise dimensional integrity. This implies that deep, narrow, high-aspect grooves may be printable in principle yet undesirable in practice if they require extensive support contact or risky post-processing [26]. Since many AM electrical-machine components reach final functional tolerances through finishing operations, slot depth and surface-feature placement must account for turning/grinding allowances so that functional grooves are not removed or rounded beyond usefulness [14]. Finally, production practicality matters: patterns that appear electromagnetically superior may be unacceptable if they impose disproportionate build time or post-processing effort [14], [29]. In this thesis, these AM considerations are reported as context only and are not used as quantitative selection metrics.

2.4.2 Mechanical Considerations for Slotted AM Rotors

Surface structuring in the rotor rim must be assessed under centrifugal loading, because high-speed rotation increases stress and amplifies stress concentration at groove roots. AM rotor studies indicate that geometry choices can influence stress distributions and enable thinner features, but mechanical behavior depends on both geometry and the material state achieved by process parameters and heat treatment [26], [30], [31]. In the present work, structural validation is not performed; mechanical considerations are therefore acknowledged but left for future work.

2.4.3 Definition of Evaluation Criteria for This Work

To ensure a fair comparison, slot-pattern candidates are evaluated under a fixed and transparent criterion set and a consistent simulation setup [30], [32], [33].While AM practicality is relevant in general [26], [29], the quantitative comparison in this thesis is based on electromagnetic indicators:

• Rotor eddy-current loss (primary): rotor loss component P_r (or an equivalent rotor loss extracted from simulation) reported consistently across candidates [20], [34].

• Torque metrics: mean torque and torque ripple (or an equivalent fluctuation metric), computed under identical operating conditions across candidates [34].

Accordingly, the results in later chapters should be interpreted as comparative electromagnetic trends across slot patterns rather than as final manufacturable designs.

FEM

3.1 FEM Setup

The Finite Element Method (FEM) is used in this work as the primary numerical framework to model and solve the three-dimensional electromagnetic field problem of the considered rotating electrical machine. FEM is particularly suitable for electric-machine analysis because it can accurately handle complex geometries (e.g., slots and end effects), spatially varying material properties, and nontrivial boundary conditions such as periodicity and motion interfaces.

In FEM, the physical domain is discretized into a finite set of small elements. Within each element, field variables are approximated by interpolation functions, and the global solution is obtained by assembling all element-level contributions into a system of algebraic equations. This approach enables the numerical solution of electromagnetic problems that are analytically intractable due to geometric and material complexity.

Electromagnetic Field Formulation

For rotating electrical machines operating at power frequency (e.g., 60 Hz), the electromagnetic behavior can be modeled using Maxwell's equations under a magneto-quasistatic assumption, where displacement current is typically negligible compared with conduction current in conductive regions. The governing curl equations can be written as

$$\nabla \times \mathrm{E} = -\frac{\partial \mathrm{B}}{\partial t}$$

$$\nabla \times \mathrm{H} = \mathrm{J}$$

where:

- Eis the electric field strength,
- Bis the magnetic flux density,
- His the magnetic field strength,
- Jis the current density.

The constitutive relations are introduced as

$$\mathrm{B} = \mu \mathrm{H}, \mathrm{J} = \sigma \mathrm{E}$$

where $\mu$is the magnetic permeability and $\sigma$is the electrical conductivity.

In transient electromagnetic analysis, time dependence is essential because induced effects such as eddy currents are driven by time-varying fields. In conductive regions, the current density is related to the electric field through $\mathbf{J} = \sigma \mathbf{E}$, and the associated Joule-loss density is given by J^2/σ. In the present thesis, these

quantities are introduced here only to define the electromagnetic modeling framework. Their quantitative evaluation and comparison are presented later in Chapter 4, whereas the present chapter is limited to model definition and simulation setup.

Software Environment: JMAG

All FEM simulations in this work are carried out using JMAG, which provides an integrated environment for the electromagnetic analysis of rotating electrical machines. In the present study, JMAG is used for geometry handling, material assignment, motion definition, boundary-condition setup, mesh generation, transient solution, and post-processing of the main electromagnetic quantities.

The purpose of the FEM setup in this chapter is to establish a repeatable and controlled simulation procedure in which the only intentional design variation between cases is the rotor slot pattern. All other modeling settings, including materials, excitation, boundary conditions, mesh policy, and solver settings, are kept consistent across cases in order to ensure a fair and traceable comparison.

3.1.1 Reference Machine Model and Operating Conditions

Reference Machine Assembly

The reference model is a full 3D electrical-machine assembly, including:

- rotor (the component under design modification),
- stator core,
- three-phase stator windings.

Although the complete machine assembly is defined at this stage, the comparative investigation in this thesis is focused specifically on how rotor surface patterning influences the electromagnetic response under otherwise unchanged conditions.

Geometry and configuration

The machine is configured with a 24-slot rotor and a 4-pole magnetic structure. The rotor dimensions are:

- Rotor outer diameter: 18 mm
- Axial length: 90 mm

These values define the baseline geometry from which all slot-pattern variants are derived.

Operating point and excitation

The motor is simulated at a mechanical speed of 1800 r/min. The electrical excitation is applied as a three-phase (U–V–W) supply at 60 Hz, implemented in a transient framework to capture time-varying electromagnetic effects. Phase currents are defined with the conventional 120° phase displacement between

U, V, and W, consistent with standard three-phase machine operation.

Material definitions and key assumptions

- Windings: The stator windings are assigned Copper material properties to represent realistic conductivity and current-carrying behavior.
- Rotor and stator cores: Both cores are modeled using soft magnetic material with relative permeability $\mu_r = 1000$ and isotropic behavior (uniform properties in all directions).
- Eddy-current modeling: Eddy currents are enabled in the conductive regions according to the chosen material settings. In particular, the material configuration includes Allow Eddy Current with electrical conductivity $\sigma = 1.05\ MS/m$ for the defined conductive magnetic material setup, consistent with the simulation settings used for this study.

These assumptions are intentionally chosen to isolate the impact of geometric slot patterning on electromagnetic response while keeping material behavior consistent across all compared cases.

These assumptions are intentionally chosen to isolate the impact of geometric slot patterning on electromagnetic response while keeping material behavior consistent across all compared cases. Figure 3.1 shows the complete 360° geometry of the reference machine assembly used to define the baseline configuration.

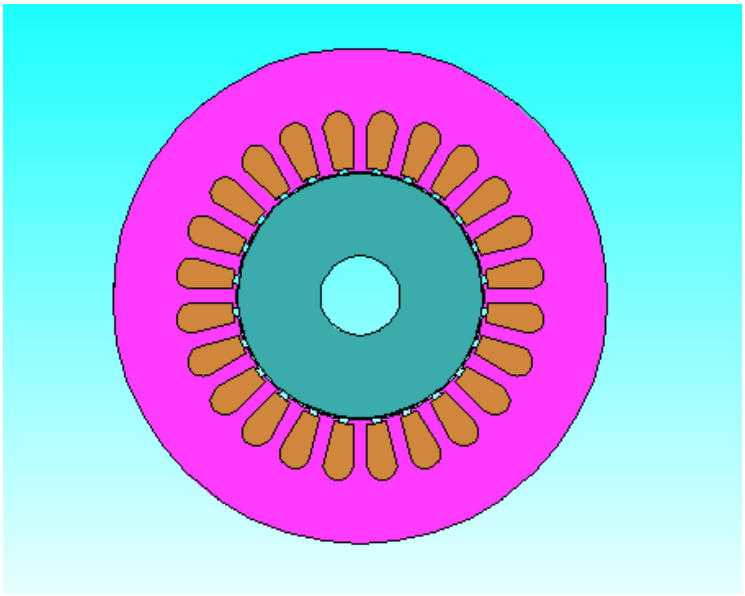

Figure 3.1 presents the complete geometry of the motor assembly, including the rotor, stator, and windings, as used for defining the reference configuration.

3.1.2 Model Definition and Boundary Conditions

A full 3D simulation of a complete model fcan be computationally expensive due to the high number of degrees of freedom and the need for small time steps in transient analysis. To reduce computational cost while maintaining physical accuracy, the model is reduced to a 90° sector (one-quarter model) by exploiting the machine's rotational symmetry.

This reduction is particularly suitable for machines with periodic electromagnetic and geometric structure, because the field solution in one sector can represent the behavior of the entire machine if appropriate periodic boundary conditions are applied. For the 4-pole structure, a 90° sector is consistent with pole symmetry and enables a significant reduction in simulation time and memory usage.

Computational domain components

The 90° sector model includes:

- rotor sector (with the baseline or patterned slot geometry),
- stator sector,
- winding regions corresponding to the sector model,
- surrounding air region (as required for field solution and boundary placement).

The rotating motion is defined such that the rotor region rotates relative to the stator region using the software's rotating machinery setup (e.g., rotating region / moving interface), ensuring that electromagnetic coupling under rotation is properly represented.

Boundary conditions

(1) Rotational periodic boundary condition

A rotational periodic boundary condition is applied on the two radial cut faces of the 90° sector. This condition enforces continuity of the electromagnetic field solution across the sector boundaries and mathematically reconstructs the full 360° behavior by linking the field variables with a 90° rotational transformation.

Applying rotational periodicity ensures that:

- the solution remains consistent with the full machine symmetry,
- artificial discontinuities at the sector boundaries are avoided,
- the computational cost is reduced without sacrificing solution fidelity.

(2) Outer boundary condition (field confinement / truncation)

Since electromagnetic FEM problems require a finite computational domain, an outer boundary is introduced

around the machine. To prevent non-physical flux leakage and to obtain a well-posed solution, the outer boundary of the surrounding region is assigned a field confinement condition (commonly implemented as a magnetic insulation / flux-parallel type boundary in electromagnetic solvers). The boundary is placed sufficiently far from the active region to minimize truncation effects.

Winding representation (*FEM Coil*)

The stator windings are modeled using *FEM Coil*, which enables direct coupling between circuit excitation and the electromagnetic field. The three-phase coil groups U, V, and W are defined and excited in transient mode. This modeling strategy ensures accurate representation of:

- coil current distribution,
- linkage between phase excitation and air-gap flux,
- induced effects in rotor regions resulting from time-varying fields.

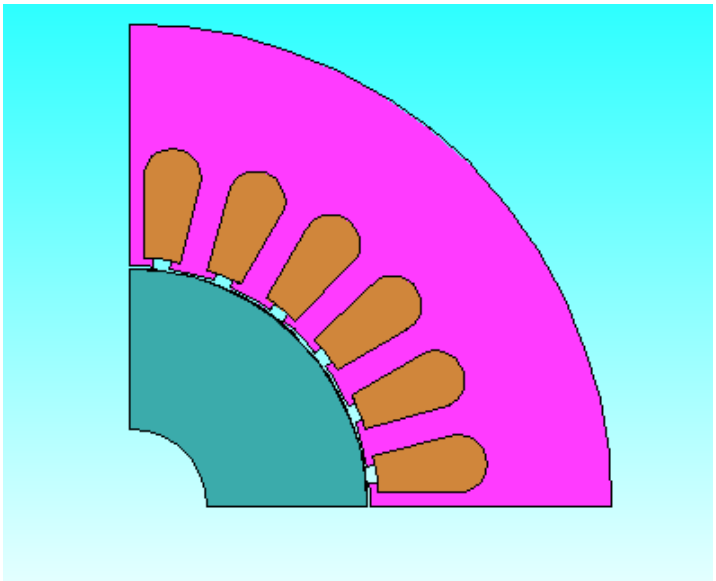

Figure 3.2 shows the adopted 90° sector model, including the ***periodic faces*** and the reduced geometry used for all simulation cases in this thesis.

3.1.3 Meshing Strategy and Numerical Settings

This section presents the meshing strategy and numerical settings adopted for the 3D transient electromagnetic simulations in JMAG. The objective is to establish a stable and repeatable computational setup. Therefore, the same meshing rules and solver settings are applied consistently to all rotor slot-pattern cases so that any differences reported later can be attributed to geometry variations rather than numerical inconsistencies.

A sliding-interface meshing approach is employed using Slide Mesh with a defined rotational motion. This

technique is well-suited for rotating electrical machines because it allows the rotor to rotate relative to the stator while maintaining consistent discretization across the motion interface. The mesh is generated using the Extruded Mesh method, which is advantageous for electric-machine geometries with a dominant axial direction because it produces layered elements along the machine length and typically improves robustness in 3D transient analyses. To preserve local geometric details during extrusion, the option to prioritize the extrusion of fillet and taper features is enabled.

Mesh resolution is controlled using element-size definitions at different geometry levels. A part-based element size of 0.5 mm is used as a general control, while a finer face-based element size of 0.25 mm is assigned to critical faces to locally refine the mesh in sensitive regions. In addition, the extruded mesh size is configured in automatic mode with a default extruded element size of 0.25 mm. An automatic mesh density gradient is enabled (maximum value 3.0) to ensure a smooth transition from fine regions to coarser regions and to reduce the risk of solver instability caused by abrupt element-size changes. For the slide interface, a single slide plane is used with 5 radial divisions and 360 circumferential divisions, while the axial-direction element size is set automatically. A surrounding air region is created to define a finite computational domain for the field solution, with directional model-length multipliers of 2.5 in the circumferential direction and 1.05 in both radial and axial directions. Contact recognition between parts is set to Automatic to improve interface consistency during meshing.

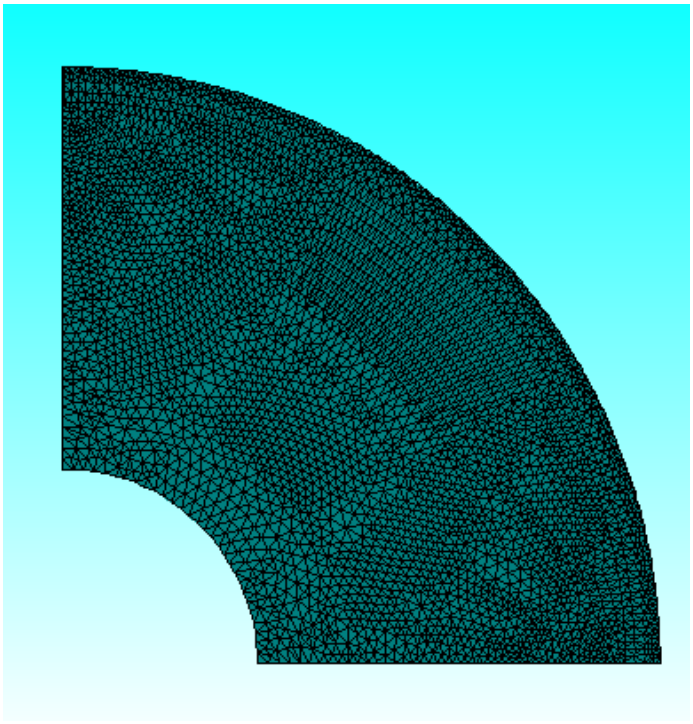

Figure 3.3. Finite-element mesh of the 90° sector model used for the 3D transient electromagnetic analysis.

The study is configured as a 3D Magnetic Field Transient Analysis using regular time intervals over one electrical period of the 60 Hz excitation. The simulation time window is defined from $t = 0\ s$ to $t = 1/60$s, and the number of steps is set to 180, resulting in a time increment of $\Delta t \approx 93.1$ μs.Prior to finalizing this setting, several candidate time-step configurations were examined to confirm adequate temporal resolution and stable convergence; based on these preliminary checks, the 180-step-per-period setting was adopted for all cases. The linear system is solved using the ICCG iterative solver with a fixed per-step convergence tolerance of $1 \cdot 10^{-8}$and a maximum iteration limit of 5000.

In addition to time-step selection, a preliminary screening study was conducted to select rotor slot dimensions before defining the final slot patterns. Several discrete values of slot depth d_s(1.0, 1.75, and 2.0 mm) and slot spacing $p_s$between circumferential ring slots (0.5, 1.0, 1.5, 2.0, 3.0, and 4.0 mm) were examined under identical modeling and numerical settings. Based on this screening, the slot dimensions used in the subsequent simulations were fixed to $d_s = 1.75$mm and $p_s = 0.5$mm. The detailed quantitative justification is presented in Chapter 4.

3.2 Smooth Rotor (Baseline Case)

The smooth-rotor case is defined as the baseline configuration used in this thesis for a controlled and fair comparison of rotor slot-patterning strategies. In the baseline model, the rotor geometry corresponds to the reference design without any additional rotor slot patterns.This baseline provides a consistent reference against which the influence of rotor patterning on electromagnetic behavior can be evaluated.

A key principle of the present study is that all modeling and numerical settings are kept identical for every case, and the only intentional design variation is the presence and type of rotor slot pattern. Therefore, the baseline case uses the same machine assembly, material definitions, boundary conditions, motion setup, meshing policy, and transient solver settings described in Section 3.1. Maintaining an identical setup ensures that later differences between cases are attributable to rotor patterning rather than differences in computational conditions.

The transient simulation produces time-domain waveforms of electromagnetic torque and rotor Joule loss. In this thesis, case-to-case comparison is performed using time-averaged values rather than instantaneous values. Accordingly, the mean torque and mean rotor Joule loss are obtained as integral averages over the selected electrical period. Quantitative values and comparisons for the baseline case and patterned rotors are presented in Chapter 4.

Figure 3.4 shows the baseline rotor geometry used as the reference for the subsequent slot-pattern configurations.

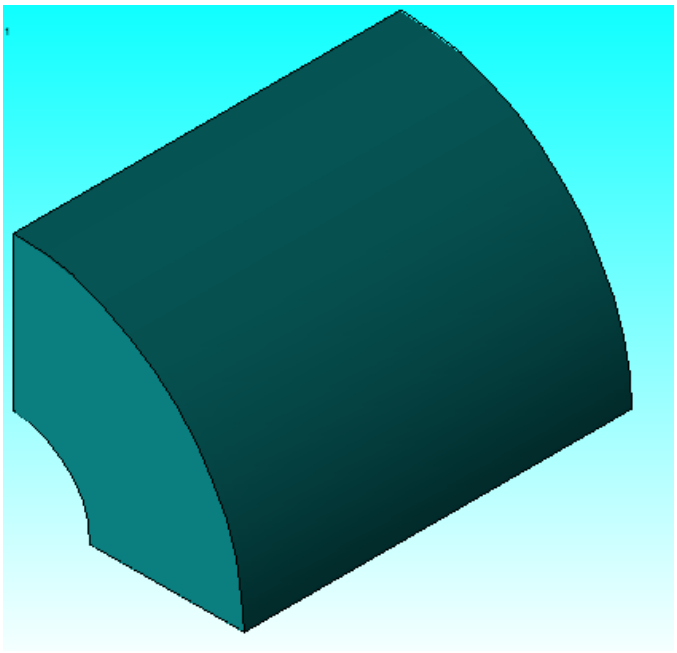

Figure 3.4. Baseline rotor geometry used in the simulations.

3.3 Axial Slot Pattern

The axial slot pattern is introduced as the first rotor-surface modification examined in this thesis. In this configuration, the rotor outer surface is segmented by a sequence of circumferential ring slots that wrap around the rotor circumference and are repeated along the axial direction. This geometry is intentionally simple and manufacturable, and it provides a clear reference case before investigating more complex pattern trajectories in later sections.

The pattern is applied using the same 90° sector model adopted for the baseline case. The ring-slot distribution is defined such that the periodic faces of the sector remain unchanged, ensuring compatibility with rotational periodic boundary conditions and seamless replication to represent the full 360° rotor. Only the rotor surface geometry is modified; all other model features and numerical settings remain identical to the baseline configuration.

Each ring slot is characterized by standard geometric parameters including slot depth d_s, slot width w_s, and the axial pitch/spacing $p_s$between adjacent ring slots.The slot edges are modeled as sharp corners (no fillets), consistent with the implemented geometry.

Figure 3.6 shows the implemented axial slot pattern: (a) geometry view and (b) the corresponding finite-element mesh view. The axial slot arrangement is defined on the rotor surface using the selected slot depth and axial pitch, while preserving compatibility with the adopted 90° sector model.

After applying the slot pattern, the mesh is regenerated using the same meshing strategy described in Section 3.1.3, with consistent local refinement to resolve the sharp slot edges. The transient electromagnetic analysis is performed with identical numerical settings as the baseline case. Quantitative results and comparisons are presented in Chapter 4.

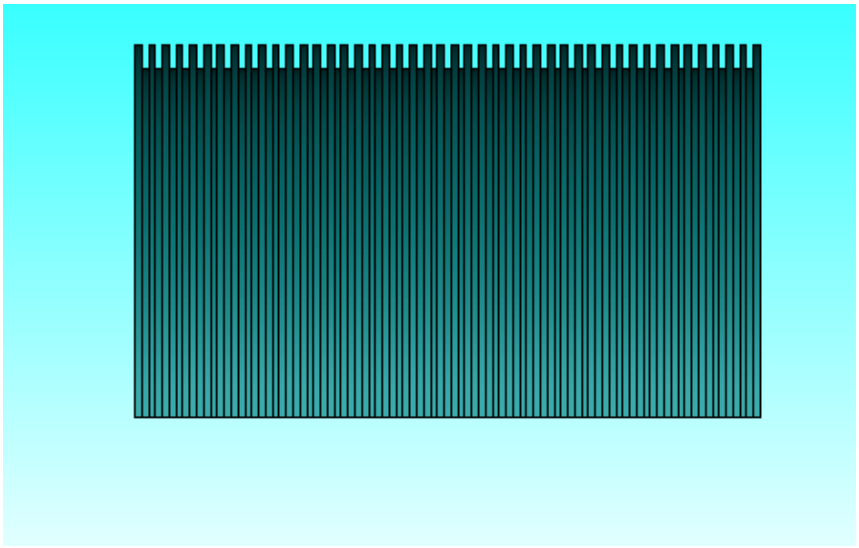

(a)

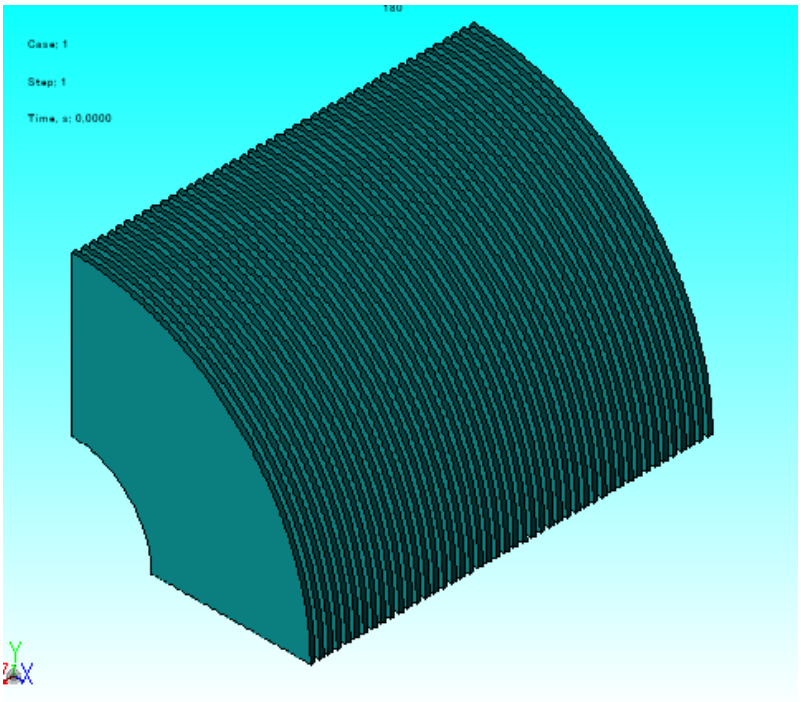

(b)

Figure 3.6: Axial slot (ring-slot) pattern applied to the rotor surface in the 90° sector model: (a) right view and (b) isometric view.

3.4 Snake-Line Slot Pattern

The snake-line slot pattern is introduced as the second rotor-surface modification strategy in this thesis. In contrast to the circumferential ring-slot pattern presented in Section 3.3, where successive slots repeat along the axial direction without an angular shift, the snake-line pattern is designed to introduce a controlled circumferential phase shift as the slotting progresses along the rotor length. The resulting trajectory is therefore not a set of circumferential rings stacked axially; instead, the slot segments appear to "wander" around the rotor surface in a snake-like path when viewed over the full axial extent. This provides a structured way to increase geometric complexity while still preserving a repeatable and CAD-friendly construction route. The snake-line geometry is implemented on the rotor outer surface within the same 90° sector modeling approach used for all cases. The key requirement is that the pattern must be compatible with the sector periodicity: the two periodic faces of the 90° model must remain clean and unchanged so that the sector can be replicated to reconstruct the full 360° rotor. The snake-line pattern is therefore created with careful control of the angular coverage of each cut and the placement of the cut features relative to the sector boundaries. Slot edges are modeled as sharp corners (no fillets), consistent with the adopted geometry assumptions used for patterned rotors in this study.

The snake-line pattern is defined such that successive slot segments follow a circumferentially shifted path along the rotor axial direction while remaining compatible with the adopted 90° sector model. In contrast to the axial ring-slot arrangement, this pattern does not preserve circumferential alignment from one axial step to the next, but instead introduces a controlled angular offset that produces the snake-line progression. A key geometric parameter is the revolve-cut angle of 89°, which is intentionally selected to be slightly smaller than the 90° sector angle. This small angular reduction preserves a narrow uncut margin and helps maintain clean periodic faces of the sector model, while enabling the circumferential offset required for the implemented slot path.

In terms of parameter consistency, the snake-line case follows the same principle used throughout this thesis: only the pattern trajectory is changed while the primary slot dimensions are kept consistent across patterned cases. These parameters define the axial repetition rate of the slot segments, while the two-plane construction and the 89° revolve angle define the circumferential shifting behavior that distinguishes the snake-line pattern from the ring-slot case. The overall result is a deterministic and repeatable geometry definition that can be replicated for other patterns under the same modeling framework.

After the snake-line geometry is created, the mesh is regenerated using the same meshing strategy described in Section 3.1.3. Because the pattern introduces sharp slot edges and additional local curvature transitions, consistent local refinement is applied around the slot boundaries to ensure adequate geometric resolution

while maintaining the same global meshing policy across cases. Particular attention is given to the regions near the slot edges where higher field gradients are expected in transient electromagnetic simulations. The transient analysis is then executed using the same numerical settings as the baseline case to ensure that the snake-line configuration differs only in rotor surface patterning and not in solver or discretization conditions.

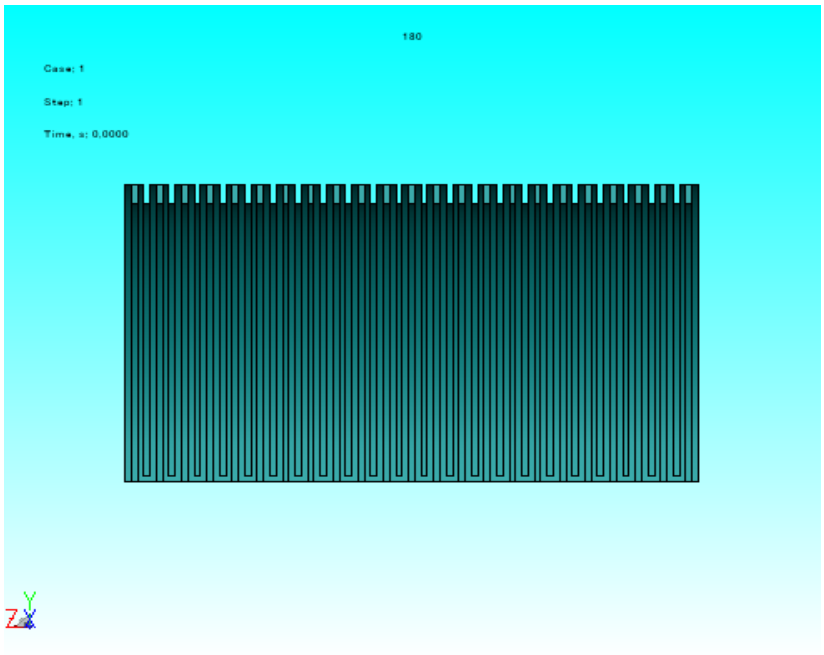

(a)

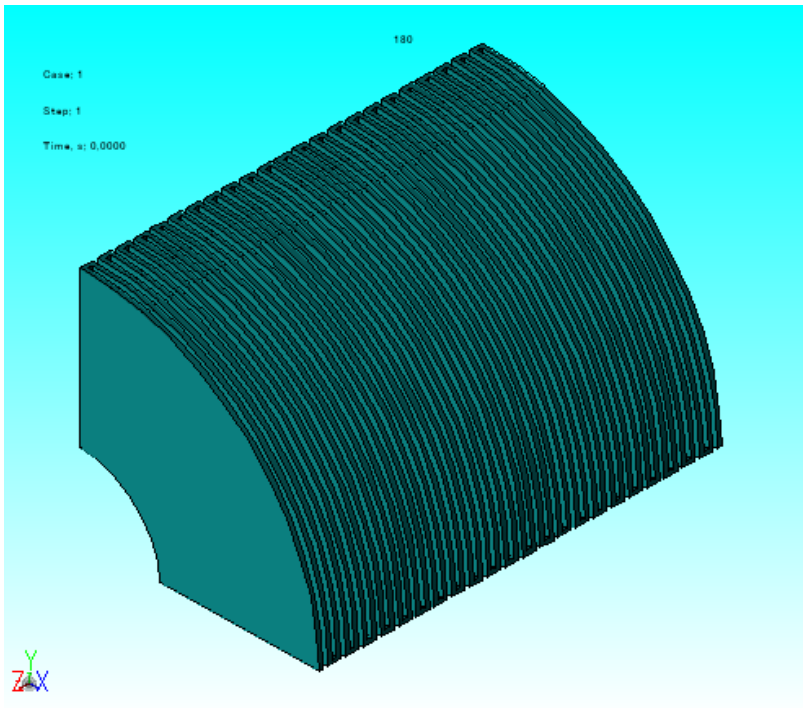

(b)

Figure 3.7: Snake-line slot pattern applied to the rotor surface in the 90° sector model: (a) right view and (b) isometric view.

3.5 Hilbert Slot Pattern

The Hilbert slot pattern is introduced as a high-complexity rotor-surface modification in this thesis. It is based on a recursive space-filling curve, in which a continuous path is generated within a bounded area through repeated directional changes at progressively smaller geometric scales. In contrast to the axial ring-slot and snake-line patterns, the Hilbert-based layout therefore produces a denser and more tortuous surface path over the rotor boundary. This characteristic makes it suitable for investigating how a more intricate form of surface segmentation influences the electromagnetic response of the rotor under otherwise unchanged modeling conditions.

From a geometric point of view, the Hilbert pattern is characterized by repeated turns, a compact path arrangement, and a high density of local corner regions. Compared with the simpler patterned configurations, this results in a more complex surface topology and a stronger local redirection of the surface path. In the present study, this type of geometry is included as a representative Hilbert-based surface pattern in order to examine the effect of increased geometric complexity within the same comparative simulation framework.

To implement the Hilbert geometry, the slot layout is generated externally in MATLAB and converted into a CAD-compatible footprint. The resulting pattern is then transferred to the rotor model and imported into the JMAG workflow for the subsequent electromagnetic simulations. Aside from the rotor surface geometry itself, the same general modeling framework, material setup, and numerical conditions are retained for consistency with the other investigated cases.

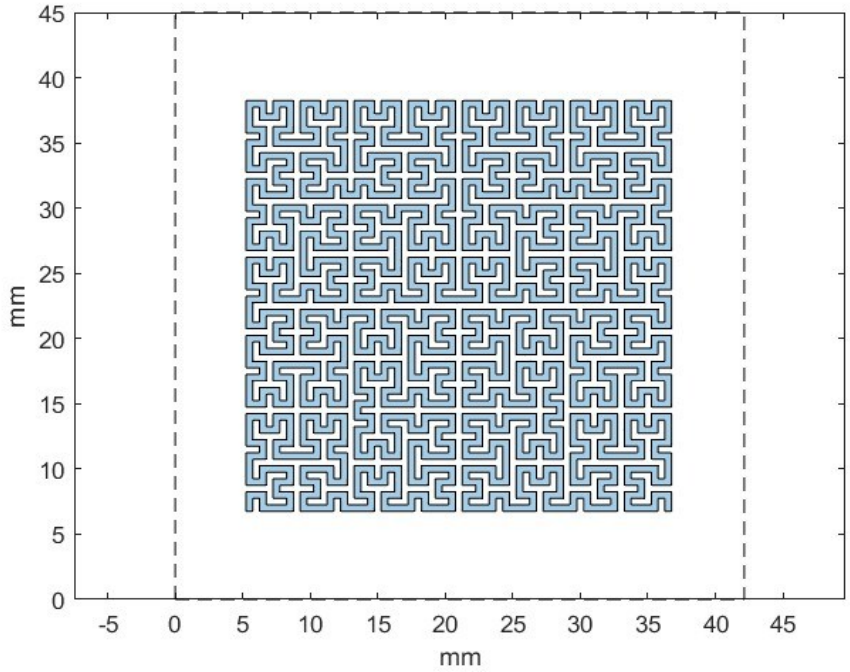

Figure 3.7: Hilbert curve footprint generated in MATLAB and exported as DXF .

The Hilbert pattern is applied to the rotor surface on the 90° sector model in order to remain consistent with the adopted periodic simulation domain. The slot layout is transferred from the externally generated footprint to the rotor surface and represented as recessed features with the same reference slot depth used for the other patterned cases, namely $d_s = 1.75\,\text{mm}$. In this way, the Hilbert configuration preserves the common geometric basis of the comparative study while introducing a substantially more intricate surface topology.

For the subsequent electromagnetic simulations, the finalized Hilbert geometry is transferred to the JMAG model in a CAD-compatible format. To ensure comparability with the baseline and the other patterned cases, the same general material definitions, motion setup, boundary conditions, meshing strategy, and solver framework are retained. Because the Hilbert pattern introduces a dense arrangement of sharp-edged recesses, local mesh refinement is applied near the slot boundaries in order to maintain adequate geometric resolution. Under this common simulation framework, the Hilbert configuration is evaluated in a manner consistent with the other investigated rotor-surface patterns.

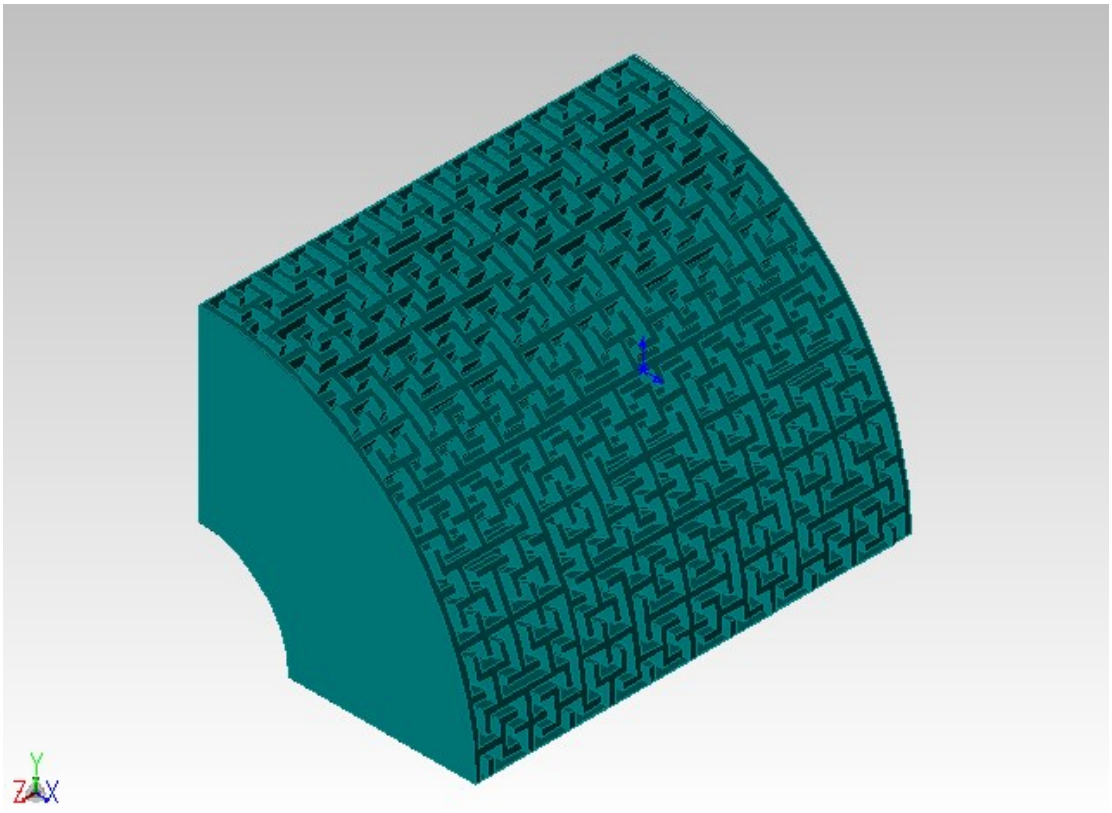

Figure 3.9: Hilbert-patterned rotor sector imported into JMAG .

Results and Discussion

4.1 Results Overview and Evaluation Approach

This chapter presents the transient 3D FEM results of the baseline rotor and the proposed rotor surface slot patterns. The objective is to quantify how different slot trajectories modify the electromagnetic response under identical operating conditions and simulation settings. All cases are solved using the same machine model, materials, boundary conditions, motion definition, meshing policy, and time-stepping configuration described in Chapter 3; the rotor surface pattern is the only intentional geometric modification.

The evaluation is based on two indicators extracted from time-domain waveforms: the electromagnetic torque $T(t)$and the rotor joule loss $P_J(t)$. Since the transient response includes an initial decay before reaching a quasi-steady behavior, the comparison is not performed using instantaneous values. Instead, integral-average values are computed over the quasi-steady portion of the response (after the initial transient decay), and the same averaging range is applied consistently to every case.

The compared configurations include the smooth rotor baseline, the axial ring-slot pattern, the snake-line pattern, and the Hilbert patterns (order 4 and order 8). For each configuration, the integral-average torque $T_{\text{avg}}$and integral-average rotor Joule loss $P_{J,\text{avg}}$are reported. Results are also expressed relative to the baseline as percentage changes to provide a compact comparison across patterns.

In addition to the averaged values, selected field visualizations are included to support interpretation. In particular, Magnetic Flux Density (Magnitude) is presented using contour and vector plots at a consistent reference time within the averaging range, allowing qualitative comparison of the field distribution among cases. The remainder of this chapter reports the results for each pattern and concludes with a consolidated comparison across all cases.

4.1 Slot-parameter selection (slot depth and slot spacing)

This section describes the preliminary parameter study performed to fix two geometric parameters that are used throughout the patterned-rotor investigations: the slot depth and the slot spacing. The purpose of this step is to reduce the number of free parameters in the later comparisons, so that differences between patterns are primarily driven by the slot-trajectory design rather than by basic slot sizing. The comparison is based on the integral-average values of electromagnetic torque and rotor Joule loss obtained from the transient simulations.

In this thesis, slot spacing (slot space) is defined as the edge-to-edge distance (gap) between two adjacent slots. The selection procedure is carried out in two stages: first, the slot depth is screened while keeping the

slot spacing fixed; then, the slot spacing is screened while keeping the slot depth fixed to the selected value.

4.1.1 Slot depth screening

To select an appropriate slot depth for the subsequent studies, a preliminary screening was performed while keeping the slot spacing fixed at 0.5 mm. Three depth values were evaluated: 1.0 mm, 1.75 mm, and 2.0 mm. For each case, both the eddy-current-related loss and the electromagnetic torque were examined using transient simulation outputs, so that the depth selection is not driven by a single metric.

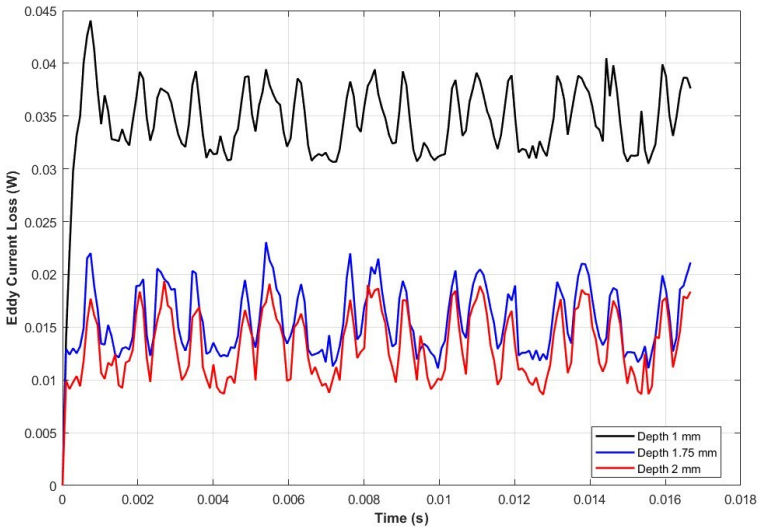

(a)

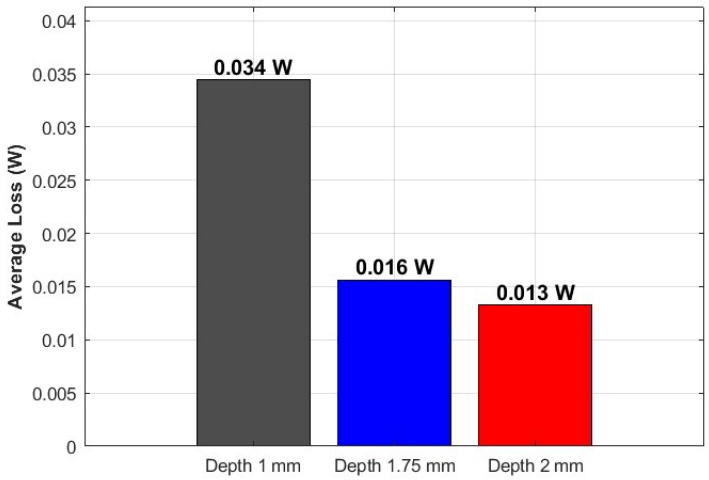

(b)

Figure 4.1: Effect of slot depth on eddy-current-related loss for a fixed slot spacing of 0.5 mm: **(a)** time-domain waveforms and **(b)** corresponding average-loss comparison.

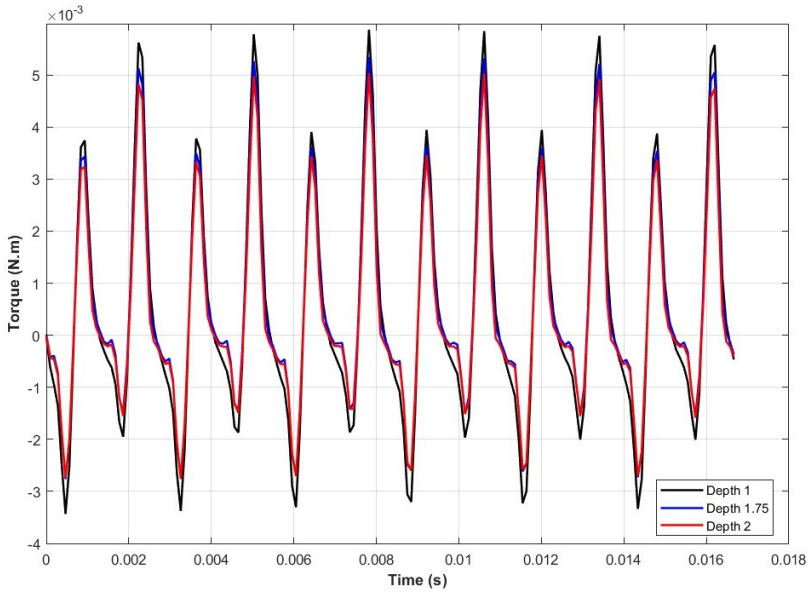

(a)

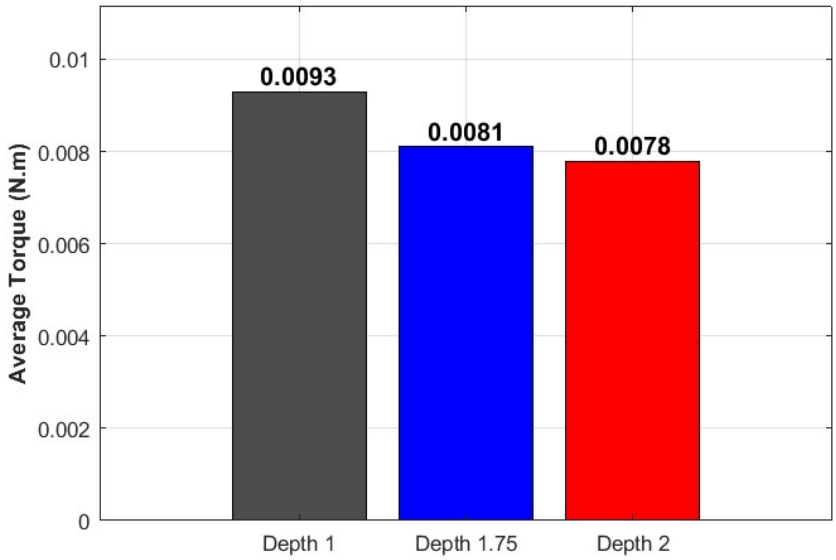

(b)

Figure 4.2**:**Torque response versus slot depth for a fixed slot spacing of 0.5 mm: (a) time-domain torque waveforms and (b) integral-average torque comparison.

Considering the eddy-current loss and torque results together, the depth cases of $d_s = 1.75$ mm and $d_s = 2.0$ mm provide the most favourable overall behaviour among the tested values. The loss comparison in Fig. 4.1 shows that moving from $d_s = 1.0$ mm to $d_s = 1.75$ mm produces a pronounced reduction in the average eddy-current loss, whereas the additional reduction obtained by

increasing the depth further to $d_s = 2.0$ mm is comparatively smaller. This indicates that the sensitivity of loss to depth becomes weaker beyond approximately $d_s = 1.75$ mm, and therefore deeper cuts yield diminishing returns in loss reduction within the explored range.

A physical explanation for this behaviour can be given in terms of skin depth. In a conductive rotor subjected to a time-varying magnetic field, the induced eddy currents are concentrated mainly within a near-surface region rather than penetrating uniformly through the full rotor body. Therefore, once the slot depth becomes comparable to the effective current penetration depth, further increasing the depth does not interrupt substantially more of the dominant current paths. As a result, the additional reduction in rotor Joule loss becomes limited, which explains the diminishing returns observed for depths beyond ds = 1.75 mm.

At the same time, the depth selection in this thesis is not based on loss alone. Slot depth also changes the rotor surface geometry and can therefore influence the electromagnetic interaction reflected in the average torque response. Figure 4.2 shows that the average torque differs between the tested depths; consequently, the depth choice must balance loss reduction against maintaining a favourable torque level. In this context,

$d_s = 1.75$ mm represents a robust compromise: it achieves the major loss reduction observed in the depth sweep while avoiding the need to adopt the maximum tested depth when the incremental loss improvement is limited.

In addition, selecting $d_s = 1.75$ mm as the reference depth is consistent with the controlled-comparison philosophy of this thesis. Since the subsequent sections focus on comparing different slot-pattern trajectories, it is beneficial to fix a depth that delivers strong loss reduction while maintaining stable average torque behaviour, so that later differences between patterns can be attributed primarily to trajectory effects rather than to an extreme depth choice. For these reasons, the depth is fixed to:

$$d_s = 1.75 \text{ mm}$$

and this value is kept constant in the subsequent slot-spacing study and in all final pattern comparisons.

4.1.2 Slot spacing screening

After selecting the reference slot depth, the second stage of the screening study focuses on the slot spacing. In this step, the slot depth is kept constant at 1.75 mm, and the slot spacing is varied over the tested values: 0.5, 1.0, 1.5, 2.0, 3.0, and 4.0 mm. For each spacing value, the transient results are processed to obtain the corresponding average loss and average torque in order to identify a suitable spacing for the subsequent pattern comparisons.

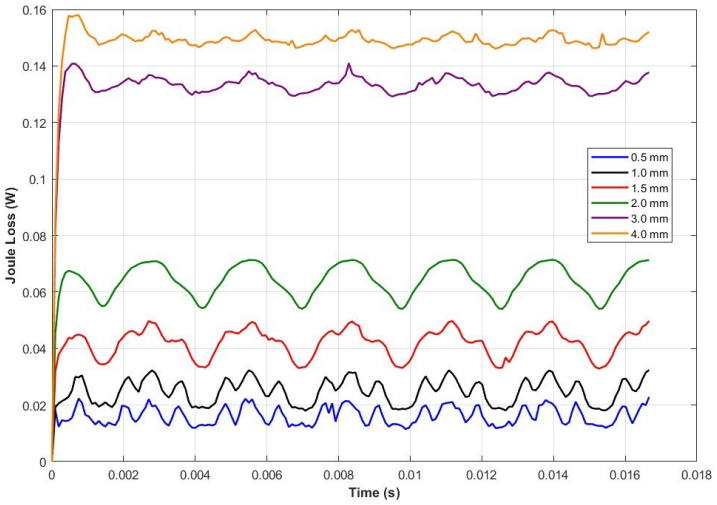

(a)

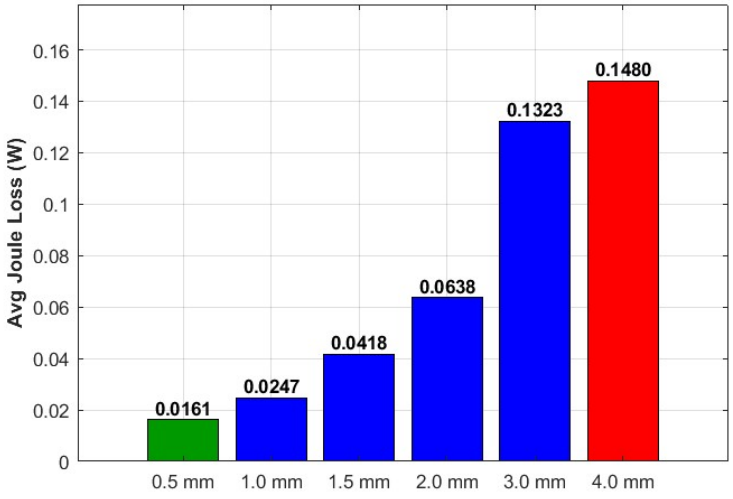

(b)

Figure 4.3: Effect of slot spacing on Joule loss for a fixed slot depth of 1.75 mm: (a) time-domain Joule-loss waveforms and (b) comparison of average Joule-loss values.

Figure 4.3 presents the Joule-loss response for different slot spacing values with the slot depth fixed at 1.75 mm. In Fig. 4.3(a), all cases show a similar periodic behaviour after the initial transient, while the loss level depends strongly on the slot spacing. Figure 4.3(b) summarizes the corresponding average joule-loss values.

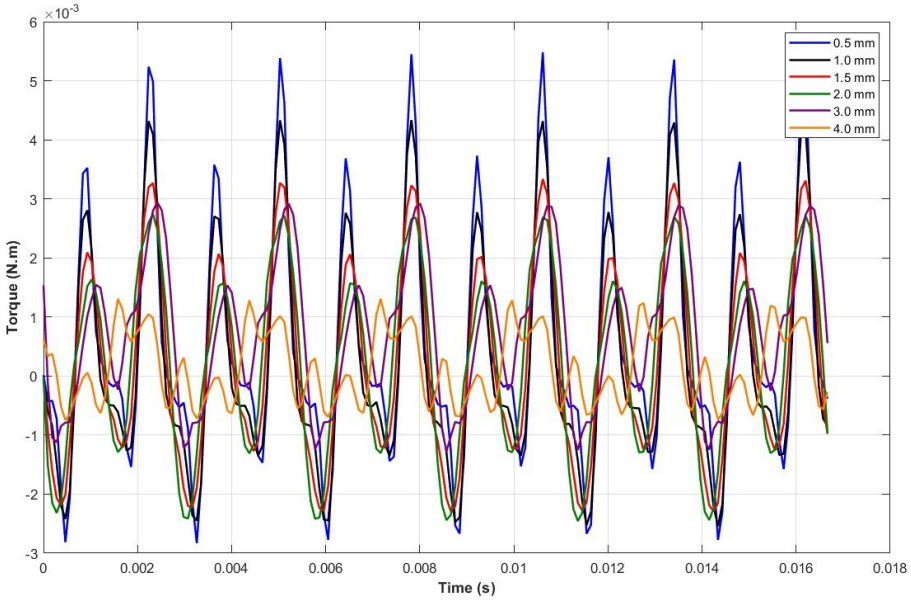

(a)

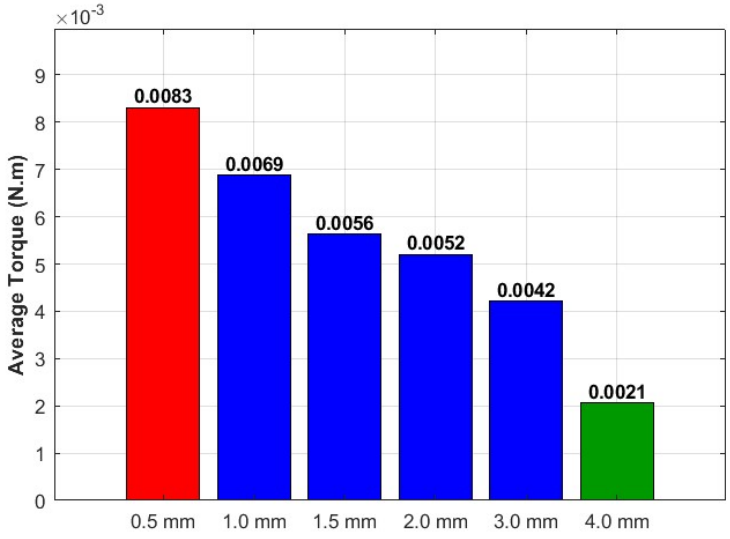

(b)

Figure 4.4: Effect of slot spacing on torque for a fixed slot depth of 1.75 mm: (a) time-domain torque waveforms and (b) comparison of average torque values.

After fixing the slot depth to 1.75 mm, the slot spacing was varied to determine a reference spacing for the remainder of the study. The spacing sweep is evaluated using both loss and torque in order to avoid selecting a spacing that improves one metric at the expense of the other. As shown by the loss results in Fig. 4.3, the average Joule loss is lowest at the smallest tested spacing and increases as the spacing becomes larger. In parallel, the torque results in Fig. 4.4 show that the average torque is highest at the smallest tested spacing

and decreases as spacing increases. Therefore, within the tested range (0.5–4.0 mm), a spacing of 0.5 mm provides the most favourable combined outcome, since it simultaneously yields the lowest average loss and the highest average torque among the evaluated cases.

In addition to its quantitative advantage, selecting 0.5 mm as the reference spacing supports a controlled comparison in the subsequent pattern studies. Fixing the spacing to the value that performs best in the preliminary sweep ensures that the later comparison between different slot-pattern trajectories is carried out under a consistent and representative geometric setting. For these reasons, the slot spacing is fixed to 0.5 mm and kept constant in all subsequent simulations.

4.2 Baseline case (smooth rotor)

The baseline case represents the smooth-rotor configuration, i.e., the rotor surface without any additional slot patterns. It is used as the reference for all subsequent comparisons in Chapter 4. The baseline and patterned cases are evaluated under the same operating conditions and numerical settings; therefore, any differences observed later can be attributed primarily to rotor surface patterning under a common modelling framework.

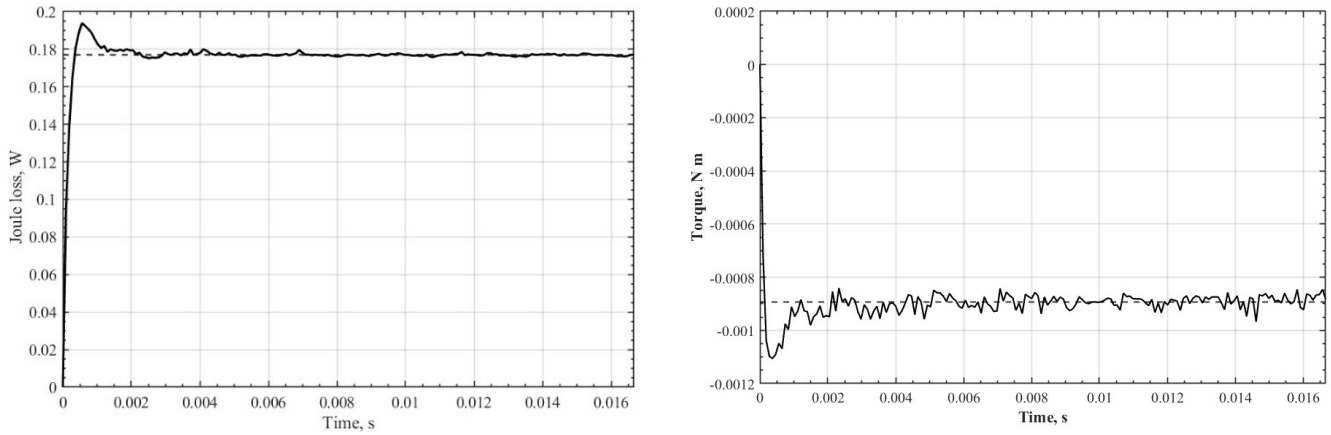

(a) (b)

Figure 4.5: Baseline transient results for the smooth rotor: (a) rotor Joule loss and (b) electromagnetic torque waveforms, including the integral-average values reported by JMAG.

In the baseline configuration, a non-zero rotor Joule loss is obtained because the conductive rotor is exposed to a time-varying magnetic field and therefore supports induced currents. The integral-average rotor Joule loss reported by JMAG is 0.1769 W, which reflects the eddy-current-related dissipation caused by induced currents in the conductive smooth rotor under time-varying magnetic excitation. The corresponding integral-average electromagnetic torque is -890 μN m, which is small in magnitude but slightly negative. This behaviour can

be explained by an eddy-current braking contribution: according to Lenz's law, induced currents generate an opposing effect to the electromagnetic excitation that produces them, and under the adopted sign convention this opposition may appear as a negative average torque. The same torque definition and sign convention are used consistently for all subsequent cases, so the baseline values provide a physically meaningful reference for the pattern comparisons.

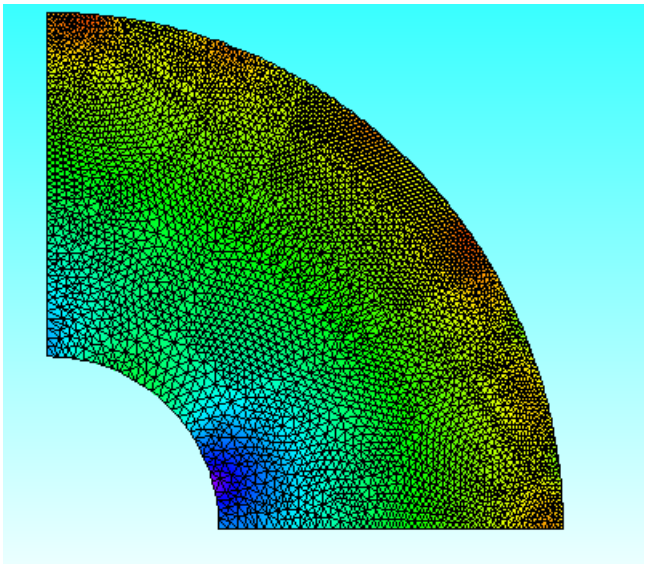

(a)

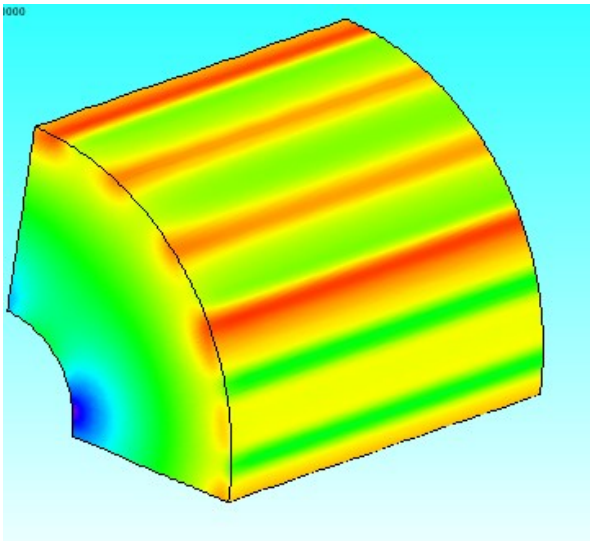

(b)

Figure 4.6: Baseline magnetic flux density magnitude $|B|$ shown as contour plots: **(a)** cross-sectional view of the 90° sector and **(b)** isometric view of the rotor sector.

Figure 4.6 shows the magnetic flux density magnitude |B| in the baseline configuration from two viewpoints.

The contour plots indicate a spatially non-uniform field distribution over the rotor surface and within the modeled sector, while the associated colour scale provides quantitative information about the local field magnitude. In this thesis, these plots are used primarily to support comparison of the field distribution between configurations.

4.3 Axial Ring-Slot Pattern

The axial ring-slot pattern represents the first patterned-rotor configuration evaluated against the smooth baseline. In this case, the rotor surface is segmented by circumferential ring slots repeated along the axial direction, while the underlying machine model, excitation, boundary conditions, mesh policy, and solver settings remain unchanged from the reference setup. The adopted geometry follows the Chapter 3 definition, with slot depth $d_s = 1.75$ mm and slot spacing $p_s = 0.5$ mm, so that the observed differences can be attributed to the surface segmentation itself rather than to changes in the numerical model.

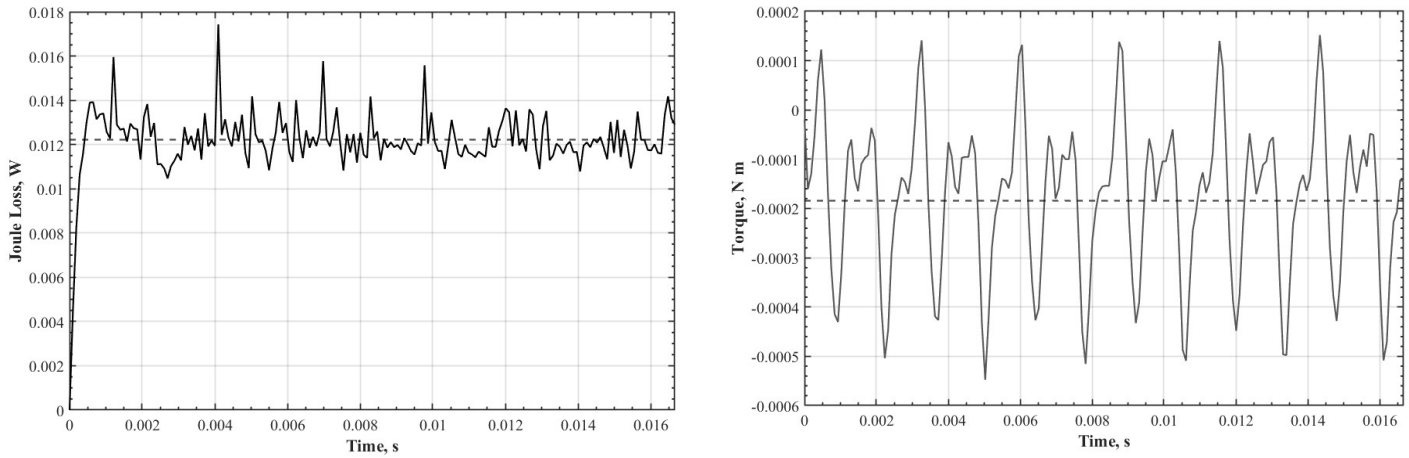

Figure 4.7. Joule loss and torque for the axial ring-slot pattern.

The transient Joule-loss and torque waveforms for the axial ring-slot rotor are shown in Figure 4.7. The integral-average rotor Joule loss is $0.0121\,\mathrm{W}$, which is substantially lower than the baseline value of $0.1769\,\mathrm{W}$. This corresponds to a reduction of approximately 93.2%, indicating that the ring-slot pattern is highly effective in suppressing rotor eddy-current-related loss under the present operating condition. The result is consistent with the intended function of circumferential surface segmentation: the slots interrupt near-surface current paths and reduce the effective area available for large circulating eddy-current loops, thereby lowering ohmic dissipation. The same figure also shows an integral-average torque of $-185\ \mu\mathrm{N\,m}$. Although the average value remains slightly negative under the adopted sign convention, its magnitude is markedly smaller than that of the smooth baseline. In absolute terms, the average torque moves closer to zero by $706\ \mu\mathrm{N\,m}$, corresponding to an approximately 79.2%reduction in braking-torque magnitude relative to the

baseline. Within the comparative framework of this thesis, this indicates that the axial ring-slot pattern not only reduces rotor loss but also mitigates the eddy-current-related opposing torque observed in the unpatterned rotor.

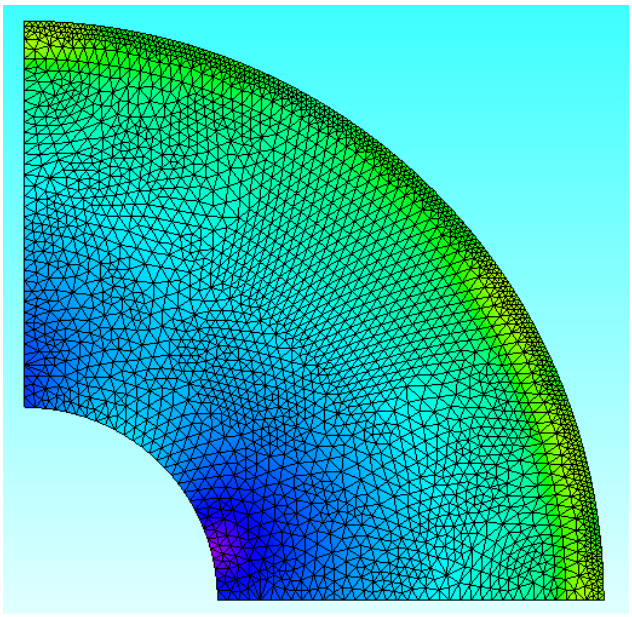

(a)

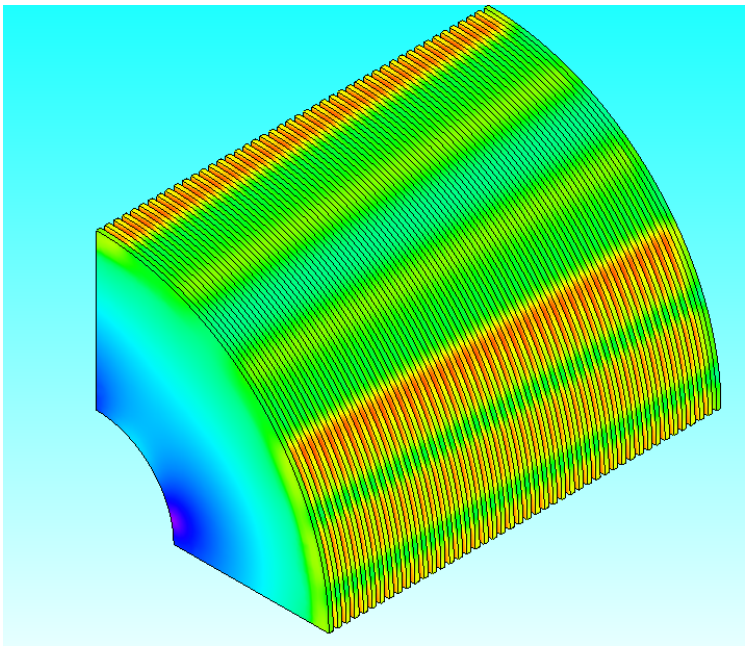

(b)

Figure 4.8. Magnetic flux density magnitude | B |for the axial ring-slot pattern: (a) cross-sectional view of the 90° sector and (b) isometric view of the rotor sector.

Figure 4.8 provides a qualitative view of the magnetic flux density magnitude |B| for the axial ring-slot case. From both the cross-sectional and isometric contour views, the field remains spatially non-uniform over the

rotor sector, but the slotted outer surface introduces a visibly segmented interaction region along the rotor periphery. In physical terms, the pattern does not eliminate the electromagnetic coupling between stator and rotor; rather, it modifies how the induced currents can close within the conductive surface layer. This explains why a strong reduction in Joule loss can be achieved while preserving a comparable overall field distribution at the machine scale. Taken together, these results show that the axial ring-slot pattern is highly effective as a first surface-segmentation strategy. Among the cases examined so far, it provides a clear improvement over the smooth rotor in both primary comparison metrics: rotor Joule loss is drastically reduced, and the average torque shifts closer to zero under the same sign convention. This makes the axial ring-slot rotor an appropriate reference patterned case for comparison with the more geometrically complex snake-line and Hilbert configurations discussed in the following sections.

4.4 Snake-Line Pattern

The snake-line pattern introduces a different surface-segmentation concept from the axial ring-slot case. Rather than repeating circumferential slots uniformly along the rotor length, this geometry incorporates an axial progression combined with circumferential phase shifting, as defined in Chapter 3 through the two-plane construction and revolve-cut procedure. Under the same simulation framework used for all previous cases, the resulting differences can therefore be attributed to the altered current-path geometry imposed by the snake-line surface pattern.

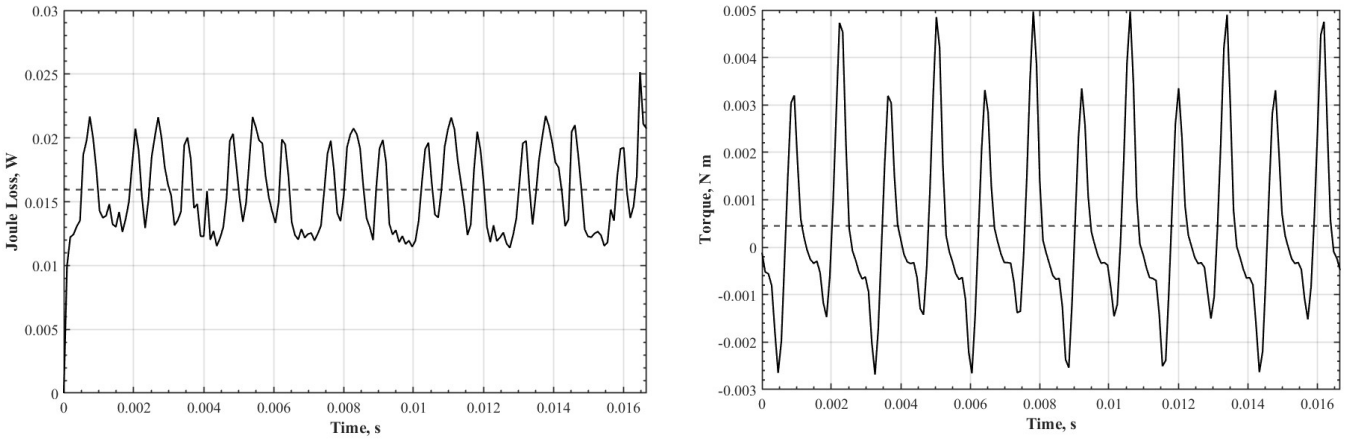

Figure 4.9. Joule loss and torque for the snake-line pattern.

The transient Joule-loss and torque waveforms for the snake-line rotor are shown in Figure 4.9. The integral-average rotor Joule loss is $0.0163\,\mathrm{W}$, which remains far below the baseline value of $0.1769\,\mathrm{W}$ and corresponds to a reduction of about 90.8%. Compared with the axial ring-slot case, however, the loss level is slightly higher, indicating that the snake-line geometry still suppresses eddy-current dissipation effectively, but not to the same extent as the simpler ring-slot segmentation. The integral-average torque is $423\,\mu\mathrm{N\,m}$,

which is positive under the adopted sign convention. Relative to the baseline value of $-891\,\mu\mathrm{N\,m}$, this represents a shift of $1314\,\mu\mathrm{N\,m}$ toward positive torque. In comparison with the axial ring-slot case, the average torque is also higher by $608\,\mu\mathrm{N\,m}$. Taken together, these results indicate that the snake-line pattern preserves the strong loss-reduction benefit of surface slotting while providing a more favourable torque response than both the smooth and axial ring-slot rotors.

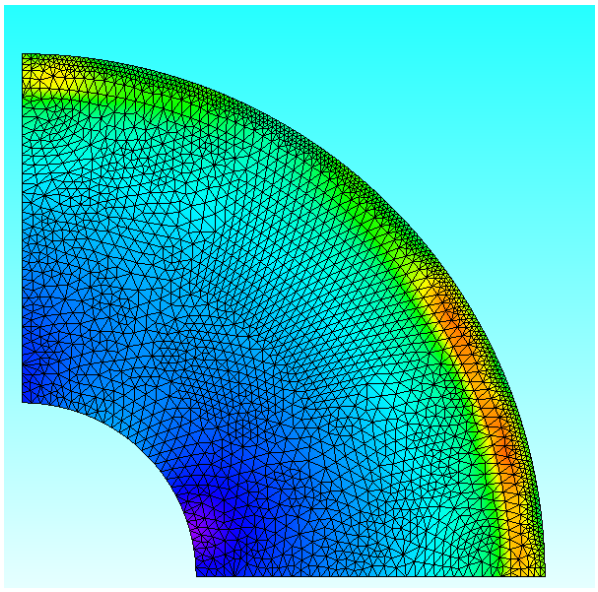

(a)

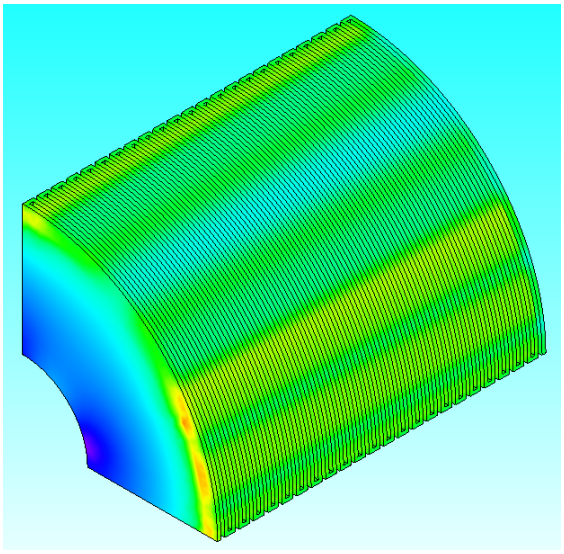

(b)

Figure 4.10. Magnetic flux density magnitude $|B|$ for the snake-line pattern: (a) cross-sectional view of the 90° sector and (b) isometric view of the rotor sector.

Figure 4.10 provides a qualitative view of the magnetic flux density magnitude $|B|$ for the snake-line case.

In both the cross-sectional and isometric contour plots, the magnetic field remains non-uniform over the rotor sector, while the patterned outer surface creates a more directionally modulated interaction region than in the purely axial slot arrangement. This suggests that the circumferential phase shift alters the way induced currents distribute and close within the conductive surface layer. The observed field pattern is therefore consistent with a configuration that still limits rotor Joule loss strongly, while at the same time shifting the average torque in a favourable direction.

Overall, the snake-line pattern represents a more balanced electromagnetic response than the smooth baseline and improves upon the axial ring-slot case in terms of average torque. Although its rotor Joule loss is slightly higher than that of the axial configuration, it remains very low in absolute terms. Within the scope of this comparative screening study, the snake-line rotor can therefore be regarded as a promising intermediate solution between simple periodic slotting and the more intricate Hilbert-type surface patterns.

4.5 Hilbert Pattern

The Hilbert pattern represents the most geometrically intricate surface-segmentation concept examined in this study. In contrast to the axial ring-slot and snake-line geometries, which impose comparatively regular surface paths, the Hilbert-based layout introduces repeated directional changes and smaller local surface features over the rotor boundary. From an electromagnetic point of view, such a configuration can alter the closure of induced currents in a more complex manner, since the surface segmentation no longer follows a predominantly axial or smoothly shifted path. Under otherwise identical model settings, the resulting response may therefore differ not only in magnitude but also in the way electromagnetic interaction is distributed over the rotor surface.

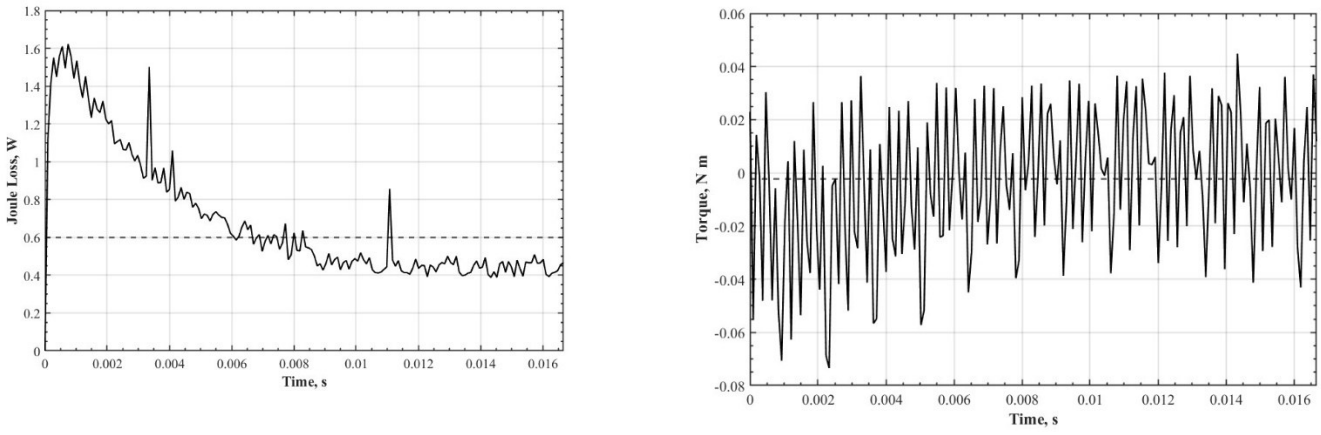

Figure 4.11. Joule loss and torque for the Hilbert pattern.

Figure 4.11 shows the transient rotor Joule loss and torque for the present Hilbert configuration. The integral-average rotor Joule loss is 0.451359 W, which is substantially higher than the corresponding values obtained

for the axial ring-slot and snake-line cases and also exceeds the smooth baseline. In relative terms, the Hilbert loss is about 155% higher than the baseline, and it is also markedly above the loss levels obtained for the two other patterned configurations. Accordingly, the present Hilbert implementation does not reproduce the loss-reduction trend observed for the previous patterned rotors. The integral-average torque is 0.00408696 N·m; however, the associated waveform exhibits pronounced oscillations over the evaluated range. For this reason, the average torque value should not be interpreted in isolation, since the strongly fluctuating transient response indicates a less regular electromagnetic behavior than that observed in the axial and snake-line cases.

A possible physical interpretation is that the Hilbert surface path modifies the near-surface current loops in a less uniform way than the simpler slotting strategies. Although surface segmentation is generally intended to interrupt large circulating eddy-current paths, the present geometry also introduces repeated turns, narrow connections, and localized directional changes. These features may promote local current crowding and more concentrated field interaction in certain regions of the rotor surface, rather than providing a uniformly beneficial interruption of current flow. In this sense, the present result suggests that increased geometric complexity does not automatically translate into improved eddy-current suppression.

At the same time, the Hilbert configuration is also expected to be more sensitive to mesh resolution than the smoother patterned cases. Because the geometry contains narrower segments and sharper directional changes, the accuracy of the numerical solution becomes more dependent on how well these local features are resolved. A dedicated mesh-refinement study for this configuration was not completed within the available project time. Therefore, the present Hilbert results should be interpreted with caution. The observed behavior may reflect both the electromagnetic influence of the pattern itself and the increased numerical sensitivity associated with the available mesh quality for this model.

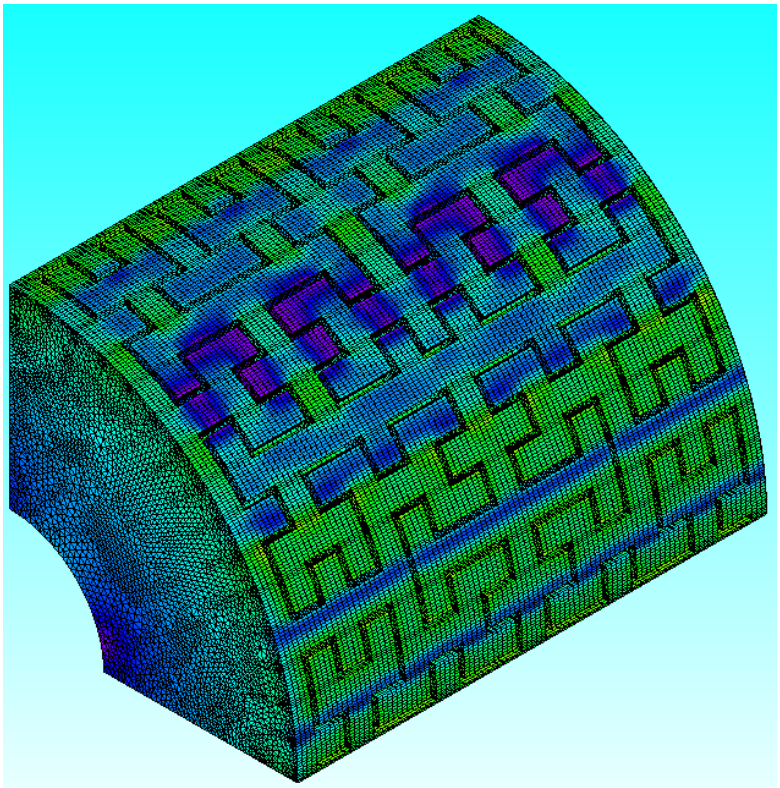

Figure 4.12. Magnetic flux density magnitude $|B|$ for the Hilbert pattern.

Figure 4.12 provides a qualitative view of the magnetic flux density magnitude $|B|$ for the Hilbert case. The contour distribution indicates a more localized field interaction along the patterned rotor surface than in the previously examined slot configurations. This observation is consistent with the idea that the Hilbert path affects the field distribution more strongly at the local level. At the same time, because this geometry is more demanding from a numerical point of view, the contour result is best interpreted as qualitative support for the altered field behavior rather than as a fully isolated explanation of the loss increase.

Overall, the snake-line pattern represents a more balanced electromagnetic response than the smooth baseline and improves upon the axial ring-slot case in terms of average torque. Although its rotor Joule loss is slightly higher than that of the axial configuration, it remains very low in absolute terms. Within the scope of this comparative screening study, the snake-line rotor can therefore be regarded as a promising intermediate solution between simple periodic slotting and more complex surface-slot trajectories.

4.6 Comparative Summary

After examining the baseline rotor and the individual surface-patterned configurations separately, a direct comparison is now useful to identify the overall performance trends of the investigated designs. Since all cases were evaluated using the same machine model, operating conditions, and numerical framework, the differences observed in rotor Joule loss and torque can be attributed primarily to the effect of the rotor surface

pattern. This comparison therefore provides the basis for assessing how effectively each geometry modifies the eddy-current-related electromagnetic response relative to the smooth reference rotor.

Configuration	Integral-average rotor Joule loss (W)	Integral-average torque (mN m)
Smooth baseline	0.1769	-0.891
Axial ring-slot	0.0121	-0.185
Snake-line	0.0163	0.423
Hilbert pattern	0.4514	4.087

Table 4.1. Comparative summary of the investigated rotor configurations.

As summarized in Table 4.1, the axial ring-slot and snake-line configurations both produce a pronounced reduction in rotor Joule loss compared with the smooth baseline. This confirms that surface segmentation of the rotor can be an effective electromagnetic strategy for limiting eddy-current-related dissipation in a solid rotor. Among the investigated cases, the axial ring-slot pattern yields the lowest rotor Joule loss, indicating the strongest loss-reduction effect within the present study. The snake-line pattern also maintains a very low loss level and, at the same time, provides the most favorable average torque response among the cases that showed clear loss improvement.

The Hilbert configuration, however, follows a different trend. In the present implementation, it does not show the same degree of Joule-loss reduction as the axial ring-slot and snake-line patterns. Instead, its loss level remains above the smooth baseline, and its torque response is accompanied by stronger transient oscillations. As discussed in the previous section, this behavior should be interpreted with caution, since the Hilbert geometry is more intricate and is therefore expected to be more sensitive to local mesh resolution and numerical accuracy than the smoother patterned cases. For this reason, the Hilbert result is retained as an informative comparative case, but not with the same level of confidence as the axial and snake-line configurations.

From the perspective of the thesis objective, the comparison in Table 4.1 highlights the main outcome of this work: rotor surface slotting can significantly influence eddy-current-related electromagnetic behavior, but its effectiveness is strongly pattern-dependent. The results show that introducing surface features alone is not sufficient; rather, the geometric form of the pattern determines whether the induced-current paths are interrupted in a beneficial way. Within the investigated design set, the axial ring-slot and snake-line patterns demonstrate clearer improvements under a consistent simulation framework, whereas the more geometrically complex Hilbert layout does not provide the same response under the present modeling conditions.

Overall, the comparative analysis supports the conclusion that structured rotor surfaces are a promising design

direction for reducing rotor eddy-current losses in additively manufactured solid rotors. At the same time, the results indicate that simpler or moderately complex slotting concepts may provide more reliable electromagnetic benefits than highly intricate surface paths. This comparative outcome forms the basis for the final conclusions drawn in the following chapter.

4.7 Conclusions and Outlook

This thesis investigated the electromagnetic effect of rotor surface slotting in an additively manufactured solid rotor using a consistent three-dimensional transient FEM framework in JMAG. The study was motivated by the fact that additively manufactured solid rotors offer increased geometric freedom, but are also more susceptible to eddy-current formation than conventional laminated structures. Within this context, the work aimed to evaluate whether rotor surface slotting can reduce rotor eddy-current-related losses while maintaining an acceptable electromagnetic response.

A smooth rotor was first defined as the baseline configuration and then compared with three representative surface-pattern concepts: an axial ring-slot pattern, a snake-line pattern, and a Hilbert-type pattern. In order to ensure a fair comparison, all cases were evaluated using the same machine model, excitation, material framework, boundary treatment, and numerical settings, such that the rotor surface geometry remained the only intentional design variation. A preliminary parameter study was also carried out to fix the reference slot dimensions for the patterned cases. Based on this screening, a slot depth of 1.75 mm and a slot spacing of 0.5 mm were selected for the subsequent comparisons.

The results show clearly that rotor surface slotting can significantly influence rotor Joule loss and torque response. The smooth baseline rotor produced an integral-average rotor Joule loss of 0.1769 W and a slightly negative average torque under the adopted sign convention. In contrast, both the axial ring-slot and snake-line patterns achieved a strong reduction in rotor Joule loss. The axial ring-slot configuration reduced the average rotor Joule loss to 0.0121 W, corresponding to the strongest loss suppression among the investigated cases. The snake-line pattern also performed well, with an average rotor Joule loss of 0.0163 W, while at the same time providing the most favourable average torque response among the loss-reducing configurations.These findings indicate that structured surface segmentation can effectively interrupt or modify near-surface eddy-current paths in a beneficial way.

At the same time, the study also shows that increased geometric complexity does not automatically lead to improved electromagnetic behaviour. The Hilbert-patterned rotor, which represented the most intricate surface topology considered in this work, did not reproduce the beneficial trend observed for the simpler patterns. In the present implementation, it resulted in a higher rotor Joule loss than even the smooth baseline

and showed a strongly oscillatory torque response. This suggests that the effectiveness of rotor surface slotting depends not only on the presence of surface features, but strongly on the specific trajectory, segmentation behaviour, and local geometric structure of the pattern. In addition, the Hilbert result should be interpreted with caution, since this geometry is expected to be more sensitive to local mesh resolution and numerical accuracy than the smoother patterned cases.

Overall, the main conclusion of this thesis is that rotor surface slotting is a promising design approach for reducing eddy-current-related losses in additively manufactured solid rotors, but its success is strongly pattern-dependent. Within the investigated design set, the axial ring-slot and snake-line patterns provided the clearest electromagnetic benefits, while the more complex Hilbert-type geometry did not show the same advantage under the present modelling conditions. The results therefore support the idea that relatively simple or moderately complex slotting concepts may offer a more reliable balance between loss suppression and electromagnetic performance than highly intricate surface paths.

The present work should be understood as a comparative electromagnetic screening study rather than a final design optimization. Several aspects remain outside the scope of the thesis, including detailed manufacturability assessment, mechanical validation under centrifugal loading, thermal coupling, and a dedicated mesh-sensitivity study for the most complex geometries. These limitations are important when interpreting the results, especially for patterns with dense local features.

Future work may therefore proceed in several directions. First, the most promising slot patterns identified here, especially the axial ring-slot and snake-line configurations, could be investigated further using refined geometric optimization and more detailed torque-ripple evaluation. Second, the Hilbert-type approach could be revisited with improved local meshing and alternative geometric scaling in order to distinguish more clearly between physical pattern effects and numerical sensitivity. Third, the electromagnetic comparison could be extended toward a broader multi-physics assessment that includes mechanical integrity, thermal behaviour, and additive-manufacturing feasibility. Such an extension would help determine which surface-slot concepts remain advantageous when practical rotor design constraints are taken into account.

In summary, this thesis provides a structured comparative basis for understanding how rotor surface slot-path geometry affects eddy-current suppression in additively manufactured solid rotors. The results confirm that surface structuring can be an effective design lever, but also show that geometric complexity alone is not sufficient; what matters is whether the selected pattern modifies induced-current paths in a physically beneficial and numerically robust manner.

References:

[1] H. Tiismus, A. Kallaste, T. Vaimann, and A. Rassõlkin, “State of the art of additively manufactured electromagnetic materials for topology optimized electrical machines,” *Additive Manufacturing*, vol. 55, p. 102778, Jul. 2022, doi: 10.1016/j.addma.2022.102778.

[2] M. Hullmann, S. Urbanek, and B. Ponick, “Surface Eddy Current Suppression on Additively Manufactured Solid Rotor Active Parts,” in *Energy Efficiency in Motor Systems*, P. Bertoldi, Ed., in Springer Proceedings in Energy. , Cham: Springer International Publishing, 2021, pp. 81–95. doi: 10.1007/978-3-030-69799-0_7.

[3] C. Klein, C. May, and M. Nienhaus, “Magnetic Performance of Eddy Current Suppressing Structures in Additive Manufacturing,” *Actuators*, vol. 13, no. 3, p. 94, Feb. 2024, doi: 10.3390/act13030094.

[4] W. Chou, Y. Liang, L. Gao, and D. Wang, “Research on eddy current losses algorithm in solid rotor of high speed squirrel cage induction motor,” *IET Electric Power Appl*, vol. 14, no. 6, pp. 1023–1029, Jun. 2020, doi: 10.1049/iet-epa.2019.0884.

[5] J. Bárta, “THE EDDY CURRENT LOSSES OF HIGH-SPEED SOLID ROTOR INDUCTION MACHINE AS FUNCTION OF THE RADIAL AIR-GAP LENGHT”.

[6] A. D. Goodall, G. Yiannakou, L. Chechik, R. L. Mitchell, G. W. Jewell, and I. Todd, “Geometrical Control of Eddy Currents in Additively Manufactured Fe-Si,” 2023, *SSRN*. doi: 10.2139/ssrn.4374024.

[7] M. Garibaldi, I. Ashcroft, N. Hillier, S. A. C. Harmon, and R. Hague, “Relationship between laser energy input, microstructures and magnetic properties of selective laser melted Fe-6.9%wt Si soft magnets,” *Materials Characterization*, vol. 143, pp. 144–151, Sep. 2018, doi: 10.1016/j.matchar.2018.01.016.

[8] B. R. Rodriguez-Vargas, G. Stornelli, P. Folgarait, M. R. Ridolfi, A. F. Miranda Pérez, and A. Di Schino, “Recent Advances in Additive Manufacturing of Soft Magnetic Materials: A Review,” *Materials*, vol. 16, no. 16, p. 5610, Aug. 2023, doi: 10.3390/ma16165610.

[9] M. Schubert and B. Ponick, “Reduction of Eddy Current Losses in Additively Manufactured Synchronous Reluctance Rotors,” in *2024 International Symposium on Power Electronics, Electrical Drives, Automation and Motion (SPEEDAM)*, Napoli, Italy: IEEE, Jun. 2024, pp. 1309–1315. doi: 10.1109/SPEEDAM61530.2024.10609070.

[10] M. Garibaldi, I. Ashcroft, J. N. Lemke, M. Simonelli, and R. Hague, “Effect of annealing on the microstructure and magnetic properties of soft magnetic Fe-Si produced via laser additive manufacturing,” *Scripta Materialia*, vol. 142, pp. 121–125, Jan. 2018, doi: 10.1016/j.scriptamat.2017.08.042.

[11] V. Bilek, J. Barta, M. Toman, P. Losak, and G. Bramerdorfer, “A comprehensive overview of high-

speed solid-rotor induction machines: Applications, classification, and multi-physics modeling," *International Journal of Electrical Power & Energy Systems*, vol. 166, p. 110520, May 2025, doi: 10.1016/j.ijepes.2025.110520.

[12] A. M. Ajamloo, H. Tiismus, A. Kallaste, M. N. Ibrahim, and P. Sergeant, "Additively Manufactured Spoke-type Permanent Magnet Rotors: Solutions to Multidisciplinary Design Challenges and Comparison with Traditional Design," *IEEE Trans. Energy Convers.*, pp. 1–12, 2025, doi: 10.1109/TEC.2025.3619827.

[13] N. Giannotta, G. Sala, C. Bianchini, and A. Torreggiani, "A Review of Additive Manufacturing of Soft Magnetic Materials in Electrical Machines," *Machines*, vol. 11, no. 7, p. 702, Jul. 2023, doi: 10.3390/machines11070702.

[14] T. N. Lamichhane, L. Sethuraman, A. Dalagan, H. Wang, J. Keller, and M. P. Paranthaman, "Additive manufacturing of soft magnets for electrical machines—a review," *Materials Today Physics*, vol. 15, p. 100255, Dec. 2020, doi: 10.1016/j.mtphys.2020.100255.

[15] Z. Wu, S. P. Narra, and A. Rollett, "Exploring the fabrication limits of thin-wall structures in a laser powder bed fusion process," *Int J Adv Manuf Technol*, vol. 110, no. 1–2, pp. 191–207, Sep. 2020, doi: 10.1007/s00170-020-05827-4.

[16] M. O. Gulbahce and D. A. Kocabas, "High-speed solid rotor induction motor design with improved efficiency and decreased harmonic effect," *IET Electric Power Appl*, vol. 12, no. 8, pp. 1126–1133, Sep. 2018, doi: 10.1049/iet-epa.2017.0675.

[17] Y. Duan, J. Zhao, Y. Xiong, H. Wang, and J. Tian, "Study on Eddy Current Loss Characteristics and Multi-Objective Optimization of High-Speed Solid Rotor Induction Motors," *Electronics*, vol. 14, no. 20, p. 4085, Oct. 2025, doi: 10.3390/electronics14204085.

[18] H. Xu, J. Zhao, Y. Xiong, and Y. Duan, "Analysis and calculation of the winding loss and rotor loss of solid rotor induction motors for flywheel energy storage system considering the influence of inverter power supply," *Journal of Energy Storage*, vol. 128, p. 117224, Aug. 2025, doi: 10.1016/j.est.2025.117224.

[19] M. O. Gulbahce, D. T. Mcguiness, and D. A. Kocabas, "Shielded axially slitted solid rotor design for high-speed solid rotor induction motors," *IET Electric Power Appl*, vol. 12, no. 9, pp. 1371–1377, Nov. 2018, doi: 10.1049/iet-epa.2018.5210.

[20] H. Xu, J. Zhao, and S. Yan, "Parameter Calculation and Rotor Structure Optimization Design of Solid Rotor Induction Motors," *Sensors*, vol. 25, no. 9, p. 2929, May 2025, doi: 10.3390/s25092929.

[21] Z. Li *et al.*, "Loss analysis of high-speed permanent magnet motor based on energy saving and emission reduction," *Energy Reports*, vol. 9, pp. 2379–2394, Dec. 2023, doi: 10.1016/j.egyr.2023.01.053.

[22] M. Zhang, S. Luo, X. Liu, and W. Li, "The eddy current loss segmentation model of permanent

magnet for temperature analysis in high-speed permanent magnet motor," *IET Power Electronics*, vol. 14, no. 4, pp. 751–759, Mar. 2021, doi: 10.1049/pel2.12009.

[23] S. Jumayev, M. Merdzan, K. O. Boynov, J. J. H. Paulides, J. Pyrhonen, and E. A. Lomonova, "The Effect of PWM on Rotor Eddy-Current Losses in High-Speed Permanent Magnet Machines," *IEEE Trans. Magn.*, vol. 51, no. 11, pp. 1–4, Nov. 2015, doi: 10.1109/TMAG.2015.2438637.

[24] Y. Lin, X. Pei, B. Yin, Z. Wu, and C. Brace, "Eddy current loss reduction technique for solid rotor high-speed surface mounted motor," in *2022 IEEE Transportation Electrification Conference and Expo, Asia-Pacific (ITEC Asia-Pacific)*, Haining, China: IEEE, Oct. 2022, pp. 1–5. doi: 10.1109/ITECAsia-Pacific56316.2022.9941885.

[25] C. Di, I. Petrov, and J. Pyrhonen, "Modeling and Mitigation of Rotor Eddy-Current Losses in High-Speed Solid-Rotor Induction Machines by a Virtual Permanent Magnet Harmonic Machine," *IEEE Trans. Magn.*, vol. 54, no. 12, pp. 1–12, Dec. 2018, doi: 10.1109/TMAG.2018.2873279.

[26] S. Urbanek *et al.*, "Design and Experimental Investigation of an Additively Manufactured PMSM Rotor," in *2021 IEEE International Electric Machines & Drives Conference (IEMDC)*, Hartford, CT, USA: IEEE, May 2021, pp. 1–6. doi: 10.1109/IEMDC47953.2021.9449566.

[27] H. T. Canseven, I. Petrov, I. Martikainen, and J. Pyrhönen, "Eddy-Current Losses in Slitted Rotor Cores of PMSMs—Development of a Novel Method," *IEEE Trans. Energy Convers.*, vol. 40, no. 2, pp. 1339–1349, Jun. 2025, doi: 10.1109/TEC.2024.3482551.

[28] P. Su, W. Hua, M. Hu, Z. Chen, M. Cheng, and W. Wang, "Analysis of PM Eddy Current Loss in Rotor-PM and Stator-PM Flux-switching Machines by Air-gap Field Modulation Theory," *IEEE Trans. Ind. Electron.*, vol. 67, no. 3, pp. 1824–1835, Mar. 2020, doi: 10.1109/TIE.2019.2902782.

[29] S. Hussain, A. Kallaste, and T. Vaimann, "Recent Trends in Additive Manufacturing and Topology Optimization of Reluctance Machines," *Energies*, vol. 16, no. 9, p. 3840, Apr. 2023, doi: 10.3390/en16093840.

[30] M. Bieber, M. Haase, F. Tasche, A. Zibart, and B. Ponick, "Additively manufactured air-cooled lightweight rotor for an automotive electric motor," in *2023 IEEE International Electric Machines & Drives Conference (IEMDC)*, San Francisco, CA, USA: IEEE, May 2023, pp. i–vii. doi: 10.1109/IEMDC55163.2023.10238918.

[31] S. Lammers *et al.*, "Additive Manufacturing of a lightweight rotor for a permanent magnet synchronous machine," in *2016 6th International Electric Drives Production Conference (EDPC)*, Nuremberg, Germany: IEEE, Nov. 2016, pp. 41–45. doi: 10.1109/EDPC.2016.7851312.

[32] P. S. Ghahfarokhi *et al.*, "Opportunities and Challenges of Utilizing Additive Manufacturing

Approaches in Thermal Management of Electrical Machines," *IEEE Access*, vol. 9, pp. 36368–36381, 2021, doi: 10.1109/ACCESS.2021.3062618.

[33] J. McKay, J. Miscandlon, and T. Konkova, "The Design and Optimization of Additively Manufactured Windings Utilizing Data Driven Algorithms for Minimal Loss in Electric Machines," *IEEE Access*, vol. 12, pp. 187406–187426, 2024, doi: 10.1109/ACCESS.2024.3509689.

[34] J. F. Gieras and J. Saari, "Performance Calculation for a High-Speed Solid-Rotor Induction Motor," *IEEE Trans. Ind. Electron.*, vol. 59, no. 6, pp. 2689–2700, Jun. 2012, doi: 10.1109/TIE.2011.2160516.